J. Fluid Mech. (2024), *vol*. 986, A11, doi:10.1017/jfm.2024.353

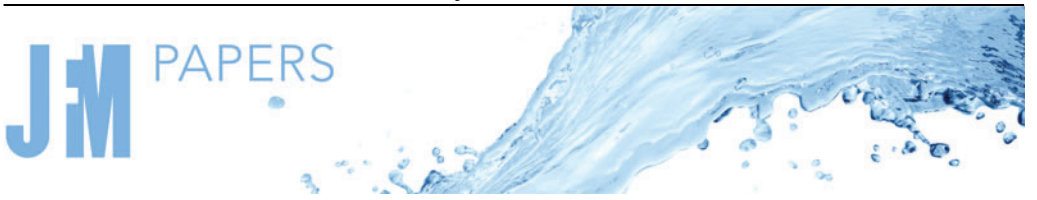

Transition induced by a bursting vortex ring in channel flow

Boyuan Wang[1] **and Yue Yang**[1,2],†

[1]State Key Laboratory for Turbulence and Complex Systems, College of Engineering, Peking University, Beijing 100871, PR China

[2]HEDPS-CAPT, Peking University, Beijing 100871, PR China

(Received 30 November 2023; revised 29 March 2024; accepted 1 April 2024)

We investigate the influence of vortices remote from the boundary on the near-wall flow dynamics in wall-bounded flows. A vortex ring with precisely controlled local twist is introduced into the outer layer of a channel flow at a moderate Reynolds number. We find that the minimum vorticity flux for triggering the transition to turbulence is significantly reduced from the initial disturbance of an untwisted vortex ring to that of a twisted ring. In particular, the latter disturbance can cause vortex bursting in the early transitional stage. The impact of vortex bursting on the transition process is characterised by the near-wall, wall-normal velocity with the rapid distortion theory. The wall-normal velocity grows during vortex bursting, and leads to streak formation and then the transition to turbulence. The notable wall-normal velocity is induced by the large di-vorticity generated in vortex bursting. We model the growing radial component of the di-vorticity in terms of the local twist, and demonstrate that its surge is due to the generation of highly twisted vortex lines in vortex bursting. Then, we derive that the generation of the di-vorticity in the outer layer enhances the wall-normal velocity in the inner layer via the Poisson equation with the image method and the multipole expansion. Thus, we elucidate that the vortex bursting can have an effect on the transition process.

Key words: vortex dynamics, transition to turbulence, topological fluid dynamics

1. Introduction

Vortex dynamics has been extensively studied in various wall-bounded flows (Adrian 2007; Wu, Ma & Zhou 2007; Farrell & Ioannou 2012; He *et al.* 2017; Luckring 2019). In particular, the hairpin vortex, consisting of a ring-like head and quasi-streamwise legs, was observed in the transition and boundary-layer turbulence (Hussain 1986; Haidari & Smith 1994; Zhou, Adrian & Balachandar 1996; Schoppa & Hussain 2002; Zhao, Yang

† Email address for correspondence: yyg@pku.edu.cn

& Chen 2016; Zhao *et al.* 2018). However, the exact role of the vortex in the transition is still not clear. Since the vortex is usually generated from the mean shear, it is difficult to distinguish its contributions. In the present study, we introduce a vortex ring, the properties of which can be controlled precisely (Shen *et al.* 2023), into a channel flow, to elucidate its effect on the transition.

Different types of disturbances were introduced near the boundary to trigger transition to turbulence, e.g. the sinusoidal velocity disturbance (Brandt & Henningson 2002), wake (Wu *et al.* 1999), puff (Rubin, Wygnanski & Haritonidis 1980; Peixinho & Mullin 2006), free-stream turbulence (Jacobs & Durbin 2001; Fransson, Matsubara & Alfredsson 2005) and various disturbances generated in experiments (Hof, Juel & Mullin 2003; Mullin 2011). Most of these methods introduce the disturbance directly into the near-wall region. However, in many transition scenarios, we only know the condition in the outer layer (with the wall unit larger than 50). For instance, the turbine blade is influenced by the vortex detached from the preceding blade. Therefore, understanding how the external vortex disturbances penetrate into the boundary (Hunt & Durbin 1999) and their induction effect near the boundary remains an open problem.

The mechanisms of the induction and penetration of external vortices jointly introduce near-wall disturbances to trigger transition (Hunt & Durbin 1999; Zaki & Durbin 2005). In the receptivity stage, external disturbances, e.g. sound waves or turbulence, stimulate instability waves within the boundary layer (Saric, Reed & Kerschen 2002; Zhong & Wang 2012). Subsequently, the instability of streaks (Ricco, Luo & Wu 2011; Wu 2019; Xu *et al.* 2023), Tollmien–Schlichting (TS) waves (Sandham & Kleiser 1992; Schlatter, Stolz & Kleiser 2004) and Λ- and hairpin-like vortices (Sandham & Kleiser 1992; Zhao *et al.* 2016) promote the transition process. Finally, the emergence of turbulent spots (Wu 2023) signals the onset of turbulence.

Distinguished from the current methods of introducing external disturbances, we employ a controllable vortex ring to induce transition. The vortex ring has been widely used as an elemental vortical structure to understand various vortical flows (Saffman 1981; Shariff & Leonard 1992; Olsthoorn & Dalziel 2015). The instability (Dazin, Dupont & Stanislas 2006), dissipation (Archer, Thomas & Coleman 2008) and axial-flow effect (Cheng, Lou & Lim 2010) of the vortex ring have been studied. However, these studies on the vortex ring are limited to the free domain without boundary conditions.

By extending the paradigm of vortex dynamics to wall flows, we analytically construct various vortex rings in the outer layer of a channel flow using the method in Shen *et al.* (2023). The construction method can precisely adjust the vorticity flux and local twist, enabling us to examine the effect of various vortex-ring properties on the transition. In particular, we construct a vortex ring with opposite chiralities to mimic the hairpin-vortex head consisting of twisted vortex lines. The collision of twist vortex waves in this vortex ring causes vortex bursting (Melander & Hussain 1994; Arendt, Fritts & Andreassen 1997; Cuypers, Maurel & Petitjeans 2003; Ji & Van Rees 2022; Shen *et al.* 2023), which can have an effect on the transition process. Furthermore, studying the vortical disturbance from the outer layer can be of importance in the control of transition.

The outline of this paper is organised as follows. Section 2 provides an overview of the initial flow set-up and numerical method. Section 3 discusses the important stages in the vortex-ring-induced transition, and characterises the effect of vortex evolution on the transition using the wall-normal velocity. Section 4 introduces the di-vorticity to explain the induction effect of the vortex ring on the wall-normal velocity. Conclusions are drawn in § 5.

2. Flow set-up and numerical overview

2.1. Initial flow set-up

The direct numerical simulation (DNS) is performed in a three-dimensional (3-D) channel domain $\mathcal{V}$ with coordinates $\boldsymbol{x} = (x, y, z) \in \mathcal{V}$ and in the streamwise x-, the wall-normal y- and spanwise z-directions, respectively. The streamwise length of the channel is $L_x = 5.61$, wall-normal height is $L_y = 2H$ with $H = 1$ and spanwise width is $L_z = 2.99$, consistent with those in the DNS in Zhao *et al.* (2016). The dimensionless 3-D incompressible Navier–Stokes (NS) equations of the velocity $\boldsymbol{u} = (u, v, w)$ scaled by H and the bulk velocity U_b read

$$\left.\begin{aligned} \frac{\partial \boldsymbol{u}}{\partial t} + \boldsymbol{u}\cdot\nabla\boldsymbol{u} = -\nabla p + \frac{1}{Re}\nabla^2\boldsymbol{u} + \boldsymbol{f}, \\ \nabla\cdot\boldsymbol{u} = 0, \end{aligned}\right\} \tag{2.1}$$

where t denotes the time, p the pressure, ν the kinematic viscosity and $Re = U_b H/\nu$ the Reynolds number. The flow is driven by a constant flux rate with $U_b = 1$ by exerting a homogeneous time-dependent body force $\boldsymbol{f} = (\tau_w, 0, 0)$, where

$$\tau_w \equiv \frac{1}{Re}\frac{\mathrm{d}\langle u\rangle}{\mathrm{d}y} \tag{2.2}$$

denotes the wall shear stress and $\langle\cdot\rangle$ the volume average.

As sketched in figure 1(*a*), periodic boundary conditions are applied in x- and z-directions, and the no-slip boundary conditions are applied at the upper boundary $y = -1$ and lower boundary $y = 1$. The initial flow field contains a vortex ring embedded in the laminar Poiseuille flow. The vortex ring serves as a controllable initial disturbance to trigger transition. The Poiseuille base flow has a velocity profile

$$u_l = U_0(1 - y^2) \tag{2.3}$$

with the centreline velocity $U_0 = 1.5$. If not otherwise specified, the Reynolds number is set as $Re = 3333$ (Kim, Moin & Moser 1987). If the flow undergoes a transition, this Re is equivalent to the friction Reynolds number $Re_\tau = Re\sqrt{\tau_w} = 207$, where τ_w is obtained in the fully developed turbulent stage. The vorticity $\boldsymbol{\omega} = \nabla\times\boldsymbol{u}$ of the base flow only has a spanwise component

$$\omega_l = 3y. \tag{2.4}$$

The vortex ring, represented by the light blue surface in figure 1(*a*), is placed at the centre of the computation domain, the farthest position from the wall. Note that the vortex ring can be placed anywhere in the outer layer. In general, the induction effect of the vortex ring on flow transition grows with the initial distance between the vortex-ring centre and the nearest wall.

The embedded vortex ring is set up using the method in Shen *et al.* (2023). The geometry of vortex lines attached on the vortex tube is sketched in figure 1(*b*). The vorticity of the vortex ring is specified as

$$\boldsymbol{\omega}(s, \rho, \theta) = \Gamma f(\rho)\left(\frac{\rho\eta}{1 - \kappa\rho\cos\theta}\boldsymbol{e}_\theta + \boldsymbol{e}_s\right), \tag{2.5}$$

where (s, ρ, θ) are curved cylindrical coordinates, $(\boldsymbol{e}_s, \boldsymbol{e}_\rho, \boldsymbol{e}_\theta)$ denote axial, radial and azimuthal basis, respectively, κ is the constant curvature of the centreline $\mathcal{C}$ of the vortex ring, Γ is the vorticity flux of the vortex ring and $f(\rho) = \exp(-\rho^2/2\sigma^2)/(2\pi\sigma^2)$ is a

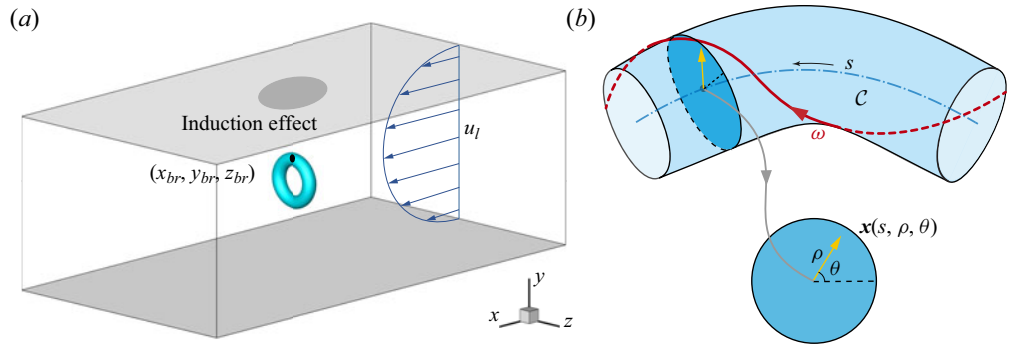

Figure 1. (*a*) Schematic of the initial flow set-up for the vortex-ring-induced transition. The grey plane denotes the solid-wall boundary of the channel flow. The vortex ring (light blue surface) is placed at the centre of the computation domain. The possible vortex bursting is located at (x_{br}, y_{br}, z_{br}), and it has a strong induction effect near the upper boundary (marked by dark grey patch). (*b*) Schematic of the vortex ring. The dash-dotted line denotes the centreline $\mathcal{C}$ of the vortex tube (light blue surface), and the red line denotes a typical twisted vortex line attached on the vortex tube. Local cylindrical coordinates (s, ρ, θ) inside the vortex tube are marked in a cross section.

Gaussian function parameterised by the standard deviation σ. Moreover, the local twist rate η measures the twisting number of vortex lines along the vortex centreline inside the vortex ring.

In the numerical construction, $\boldsymbol{\omega}(s, \rho, \theta)$ in (2.5) in curved cylindrical coordinates is mapped to $\boldsymbol{\omega}(x, y, z)$ in Cartesian coordinates using the algorithm in appendix A of Shen *et al.* (2023). Various closed vortex tubes (Shen *et al.* 2022) can be constructed with a given parametric equation for the centreline and the function $f(\rho)$ for the vorticity-flux distribution.

2.2. *Internal structures of the vortex ring*

The configuration parameters of the vortex ring are set based on the DNS result of the same channel flow in Zhao *et al.* (2016). As illustrated by the isosurface of the swirling strength λ_{ci} (Zhou *et al.* 1999) in figure 2, the head of the hairpin-like vortex tube forms a ring-like structure consisting of helical vortex lines in the late stage of the natural transition. In particular, the twist rate of vortex lines is not uniformly distributed on the vortex ring. The chiralities of the helical lines are opposite on the two halves of the ring.

Thus, we set the differential twist, i.e. the non-uniform local twist rate $\eta = A\cos(s/R)$ along $\mathcal{C}$, with the constant $A = 120$ (Shen *et al.* 2023). For comparison, we also set cases with the uniform twist $\eta = 2A/\pi$ and zero twist $\eta = 0$. The initial twist is crucial in determining whether the vortex ring will burst during its evolution (Shen *et al.* 2023). In addition, the vorticity flux Γ, vortex ring radius $R = 0.25$ and ring thickness $\sigma = 0.0125$ are comparable to the DNS result in Zhao *et al.* (2016) at $t = 110$ in the late transition. Note that the induction effect of the vortex ring on flow transition strongly depends on A, which plays a similar role as Re, whereas it weakly depends on R and σ (Shen *et al.* 2022, 2023).

2.3. *DNS*

The NS equations (2.1) are solved by DNS using the same spectral method in Kim *et al.* (1987). The velocity in the x- and z-directions is decomposed into Fourier modes,

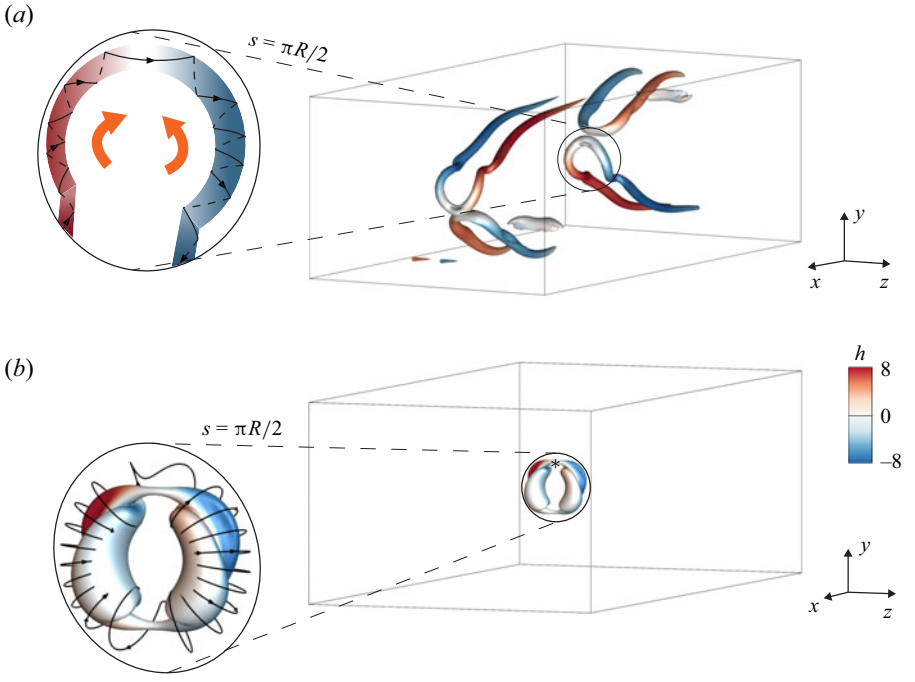

Figure 2. Modelling an external vortex in flow transition using a vortex ring. (*a*) Isosurface of the swirling strength $\lambda_{ci} = 2$ (Zhou *et al.* 1999) at $t = 110$ in the late stage of the natural transition in channel flow reported in Zhao *et al.* (2016). The isosurface is colour-coded by the helicity density $h = \boldsymbol{\omega} \cdot \boldsymbol{u}$. The hairpin head consisting of helical vortex lines is sketched in the closed-up view on the left. The orange arrows denote axial flows inside the vortex tube induced by the helical vortex lines with opposite chiralities. (*b*) Isosurface of the $\lambda_{ci} = 2$ (colour-coded by h) in the present vortex-ring-induced transition. The helical vortex lines with opposite chiralities near the vortex ring are plotted in the closed-up view on the left. The possible bursting location is marked by the asterisk at $s = \pi R/2$ in the local cylindrical coordinates.

and $\boldsymbol{u}$ in the y-direction is solved by the Helmholtz equations for each mode. The time stepping is varied to ensure the Courant–Friedrichs–Lewy number less than 0.6. The initial vorticity field, the superposition of laminar background (2.4) and vortex ring (2.5), is decomposed into Fourier–Chebyshev modes. To satisfy the boundary conditions for a channel, the initial velocity field is calculated from the vorticity via the Helmholtz equation in the Fourier–Chebyshev space. A boundary correction is then applied under the divergence-free constraint, which is detailed in Appendix A. In the calculation of flow evolution, the two-thirds truncation method is applied for dealiasing (Canuto *et al.* 1988). The low-storage third-order semi-implicit Runge–Kutta method (Philippe, Robert & Michael 1991; Yang & Pullin 2011) is used for time marching.

We performed convergence tests on four grids with $N_x \times N_y \times N_z = 768 \times 769 \times 768$, $576 \times 577 \times 576$, $384 \times 385 \times 384$ and $192 \times 193 \times 192$ grid points. After examining the convergence of the maximal vorticity magnitude for vortex evolution at $t \leqslant 1.5$ and Re_τ for flow transition at $t \leqslant 70$, we chose the grid of $384 \times 385 \times 384$ for the simulation at $Re = 3333$. We conducted an additional DNS at $Re = 8090$ on the grid of $768 \times 769 \times 768$ to study the effect of Re.

Case	η	Γ	Γ^*	$\Gamma^*/\Gamma^*_{\eta=0}$	E_t	Transition
1	$A\cos(s/R)$	0.047	0.0394	17.1 %	7.829×10^{-5}	Yes
2	$2A/\pi$	0.047	0.0812	35.2 %	7.294×10^{-5}	No
3	$2A/\pi$	0.097	0.0812	35.2 %	2.879×10^{-4}	Yes
4	0	0.278	0.2310	100 %	3.879×10^{-4}	Yes

Table 1. Parameters η and Γ of the vortex ring in four representative cases of the vortex-ring-induced transition of channel flow. The threshold vorticity flux Γ^* for triggering transition, Γ^* normalised by $\Gamma^*_{\eta=0}$ (Γ^* in Case 4) and the volume-averaged disturbance energy E_t are listed. Note that Cases 1, 3 and 4 have the transition with $\Gamma \approx 1.2\Gamma^*$.

3. Transition induced by a vortex ring

3.1. *Stages in transition process*

In this section, we demonstrate that the initially embedded vortex ring can induce transition in wall flows at moderate Re, and the critical magnitude of the initial disturbance is highly dependent on the initial twist of the vortex ring. For the vortex rings with three different η, we first examine the critical vorticity flux $\Gamma = \Gamma^*$ to induce transition. Here, Γ^* is determined by assessing whether the flow will undergo a transition through a series of simulations conducted for various values of Γ.

As listed in table 1, we set up four DNS cases for the vortex-ring-induced transition to illustrate the influence of the internal structure inside the vortex ring. In Case 1, the initial vortex ring with chirality-opposite helical structures mimics the hairpin head in the natural transition, and it has the minimum Γ^*. As shown in figure 2, the isosurface of λ_{ci} colour-coded by the helicity density $h = \boldsymbol{u} \cdot \boldsymbol{\omega}$ shows positive and negative h in the two halves of the vortex ring. In this case, we set $\Gamma \approx 1.2\Gamma^*$ to quickly trigger transition.

In Case 2, the vortex ring is the same except that the twist is uniform, and Γ^* is more than twice of that in Case 1. Thus, Case 2 has no transition with $\Gamma < \Gamma^*$. Note that Cases 1 and 2 have roughly the same disturbance energy

$$E_t = \frac{1}{V}\int_{\mathcal{V}} \frac{1}{2}((u-u_l)^2 + v^2 + w^2)\,\mathrm{d}\mathcal{V}, \tag{3.1}$$

where V denotes the volume of the channel. Therefore, the different twist distributions in Cases 1 and 2 only have a minor effect on E_t, but they have an effect on the transition process. Case 3 is the same as Case 2 except $\Gamma > \Gamma^*$, so it has transition. In Case 4, the vortex ring with $\eta = 0$ and $\Gamma > \Gamma^*$ also induces transition.

The evolution of Re_τ, indicating the variation of the wall friction, in the four cases is plotted in figure 3. It can be roughly divided into three stages. Before a characteristic time $t_1 = 1$, the major dynamics is only within the vortex ring, including the vortex bursting in Case 1. From t_1 to $t_2 = 10$, the vortex ring breaks up, and Re_τ grows mildly. From t_2 to $t_3 = 40$, Re_τ starts to surge and the transition occurs in the cases with $\Gamma > \Gamma^*$, whereas Re_τ remains at the laminar value for $\Gamma < \Gamma^*$. The flow evolution in the three stages is elaborated on in the following.

3.1.1. *Stage 1: dynamics inside the vortex ring*

Figure 4 shows the main dynamics inside the vortex ring around t_1. In Case 1, an initially helical vortex ring with differential twist has the azimuthal vorticity ω_θ, which generates

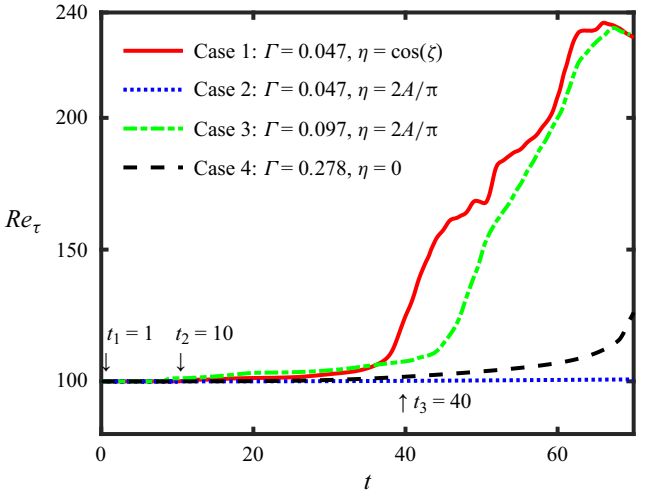

Figure 3. Temporal evolution of the wall-friction Reynolds number in various cases (listed in table 1).

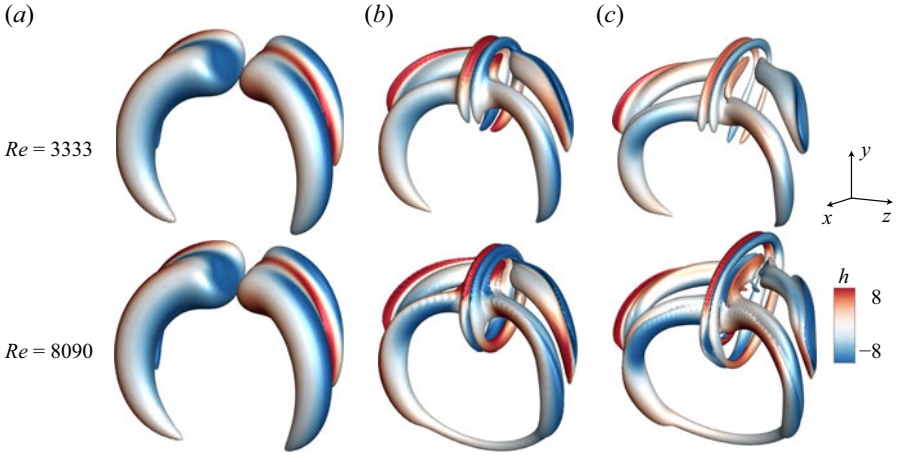

Figure 4. Evolution of the isosurface of λ_{ci} during the vortex bursting in Case 1 with two Reynolds numbers. The surface is colour-coded by the helicity density: (*a*) $t = 0.3$ and $\lambda_{ci} = 2.4$; (*b*) $t = 0.9$ and $\lambda_{ci} = 2.4$; (*c*) $t = 1.5$ and $\lambda_{ci} = 2.1$.

the axial velocity

$$u_s(s, \rho, \theta) = \frac{1}{1 - \kappa\rho\cos\theta}\frac{\Gamma}{2\pi}\exp\left(-\frac{\rho^2}{2\sigma^2}\right)\eta \tag{3.2}$$

along the vortex-ring centreline (see Appendix B for a detailed derivation). The two twist vortex waves with opposite chiralities collide at the symmetrical plane at $s = \pi R/2$. This leads to vortex bursting (Shen *et al.* 2023): a part of the vortex tube is flattened on the symmetrical plane, forming a disc-like structure with highly spiral vortex lines.

Using the vortex-ring model in Shen *et al.* (2023), the starting and ending times of the vortex bursting in Case 1 are defined as

$$t_{bs} = \frac{2\pi R}{\Gamma A} \approx 0.3 \tag{3.3}$$

and

$$t_{be} = \frac{10\pi^2 R}{3\Gamma A} \approx 1.5, \tag{3.4}$$

respectively. Figure 4(*a*,*c*) shows the vortical structures at t_{bs} and t_{be}.

Moreover, the vortices for $Re = 3333$ and 8090 are nearly identical in figure 4(*a*), because the viscosity dependence is weak at early times, consistent with the model in (3.2). In figure 4(*c*), the *Re*-effect becomes noticeable because the model in (3.2) breaks down near the bursting site with strong viscous vortex reconnection. As discussed in Shen *et al.* (2023), increasing *Re* is equivalent to increasing an effective η. A larger η in (3.2) suggests a larger u_s, leading to stronger vortex bursting with generating larger disc-like structures. By contrast, there is no bursting in Cases 2–4 for initial vortex rings with uniform or zero twist.

3.1.2. *Stage 2: breakup of the vortex ring*

Figure 5(*a–c*) illustrate the breakup dynamics of the vortex ring from t_1 to t_2 in Cases 1–3, respectively. At $t = t_1$, the initially helical vortex ring splits into primary and secondary rings due to the axial flow (Cheng *et al.* 2010). The primary vortex ring undergoes further transition, and the secondary rings dissipate before t_2. By contrast, the vortex with $\eta = 0$ in Case 4 retains its ring shape at $t = t_1$ in figure 5(*d*).

From t_1 to t_2, the vortex rings with and without the initial twist evolve very differently. For $\eta > 0$, the vortex rings experience dramatic deformation in figure 5(*a–c*). The uniformly twisted vortex ring folds and elongates under the mean shear in figure 5(*b*,*c*). This process from $t = 1$ to $t = 5$ in Case 2 is further illustrated in the side view in figure 6. The vortex ring is persistently stretched along the streamwise direction until $t = 9$, and eventually breaks up into several pairs of streamwise vortices. Although the evolutions of the vortices are similar in Cases 2 and 3, the larger Γ in Case 3 induces a transition whereas the flow relaminarises in Case 2. The ring with differential twist has a similar evolution in figure 5(*a*). Since its internal structure is already unstable at $t = t_1$, the breakup process in Case 1 is faster than in Cases 2 and 3, which agrees with the different growth rates of Re_τ in figure 3.

The vortex ring with $\eta = 0$ does not break up in stage 2. Its aspect ratio oscillates in figure 5(*d*) due to the elliptic instability (Kerswell 2002) with the ring deformation in the *x*-direction and the curvature instability (Fukumoto & Hattori 2005; Blanco-Rodríguez & Dizès 2017) with the variation of the ring curvature.

3.1.3. *Stage 3: late transition*

Cases 1–3 at t_3 in stage 3 of late transition are very similar. In figure 7 for Case 1, the inverse hairpin-like structure in figure 7(*a*) evolves into streamwise vortices in figure 7(*b*), which characterise a quasi-stable TS wave (Boiko *et al.* 1994). Then the flow evolves as in the natural transition (Zaki 2013; Zhao *et al.* 2016), i.e. from streaks to the Λ- or hairpin-like structure in figure 7(*c*), and finally it breaks down into turbulence in figure 7(*d*). Moreover, the transition follows an almost identical route at a larger $Re = 8090$, whereas the rise of Re_τ occurs much earlier than that at $Re = 3333$ (not shown).

In particular, the evolution and generation of the hairpin vortices are depicted in figure 8. The signature of hairpin vortices aligns with that in Adrian, Meinhart & Tomkins (2000) in terms of the streamwise length, wall-normal location and angle between hairpin head and neck. From $t = 31$ to $t = 34$, the primary hairpin vortex elongates streamwise, and the secondary hairpin vortex forms at the ridge of the primary one (Zhou *et al.* 1999). Then,

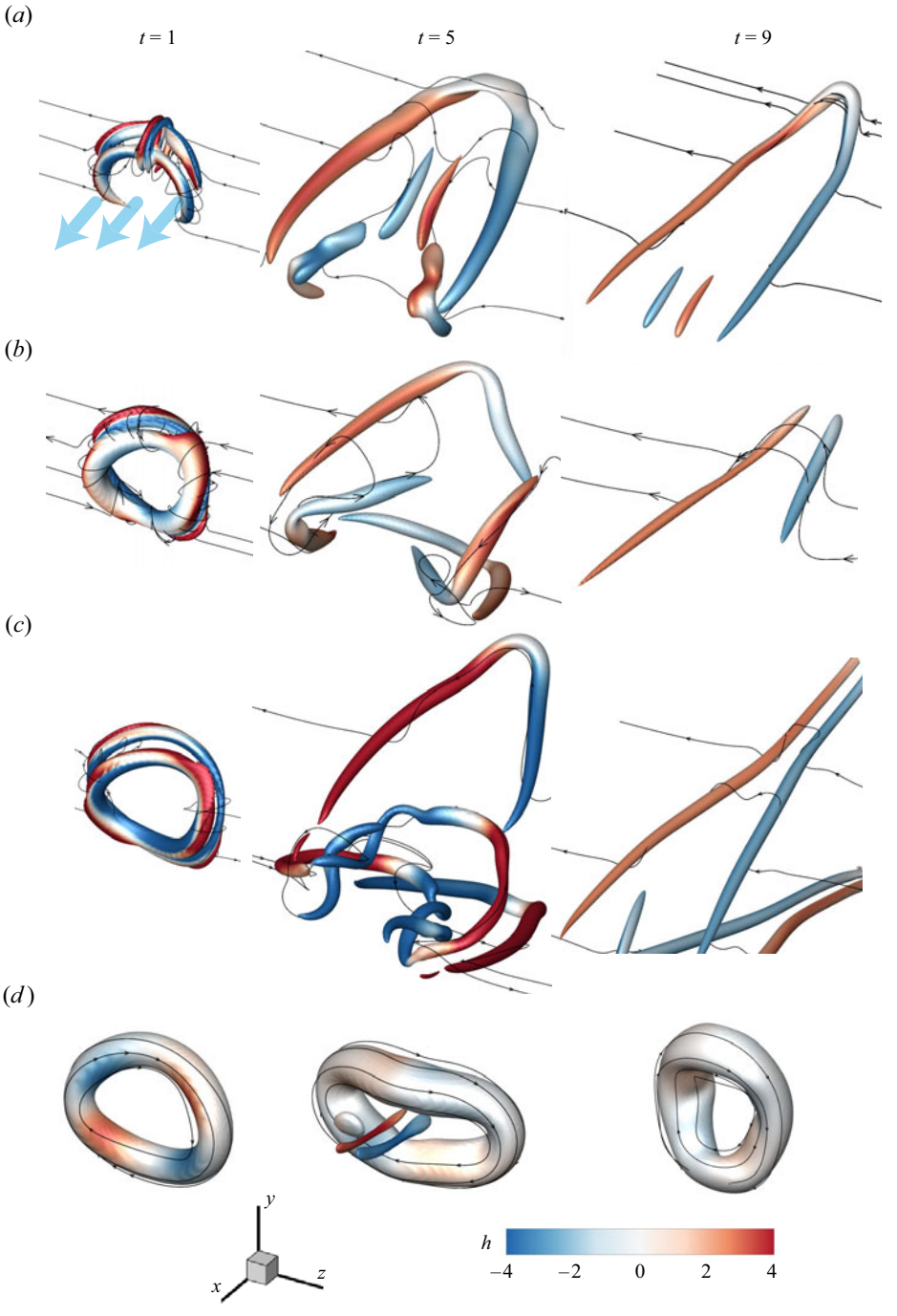

Figure 5. Evolution of the isosurface of λ_{ci} in the second stage of transition in (*a*) Case 1 with $\eta = A\cos\xi$ and $\Gamma = 0.047$, (*b*) Case 2 with $\eta = 2A/\pi$ and $\Gamma = 0.047$, (*c*) Case 3 with $\eta = 2A/\pi$ and $\Gamma = 0.097$ and (*d*) Case 4 with $\eta = 0$ and $\Gamma = 0.278$. The isocontour values in each row are $\lambda_{ci} = 2.1$ at $t = 1$ and $\lambda_{ci} = 1$ at $t = 5$ and 9. The isosurface is colour-coded by the helicity density. The blue arrows in (*a*) denote the direction of the mean flow. Black lines denote vortex lines.

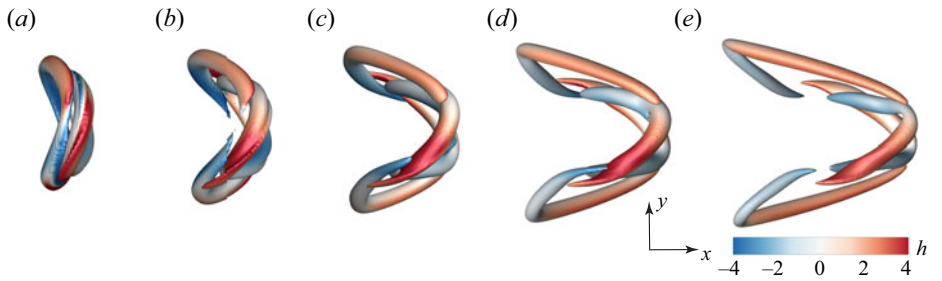

Figure 6. Evolution of the isosurface of λ_{ci} from $t = 1$ to $t = 5$ in Case 2 with $\eta = 2A/\pi$ and $\Gamma = 0.047$ (side view). The isosurface is colour-coded by the helicity density.

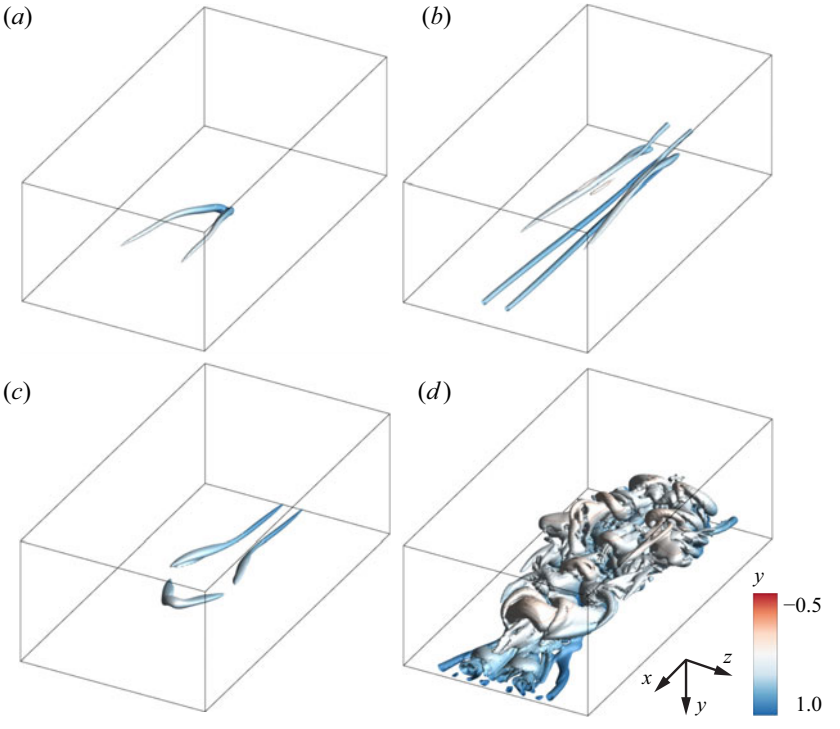

Figure 7. Evolution of the isosurface of λ_{ci} after the dissipation of the vortex ring in Case 1. The surface is colour-coded by the wall distance. Note that the channel is flipped in the y-direction for clearly showing the vortical structure: (*a*) $t = 10$ and $\lambda_{ci} = 1.3$; (*b*) $t = 20$ and $\lambda_{ci} = 0.5$; (*c*) $t = 30$ and $\lambda_{ci} = 1$; (*d*) $t = 40$ and $\lambda_{ci} = 1.3$.

more hairpin-like structures emerge at the ridges of the primary and secondary hairpins at $t = 35$, forming a coherent packet of hairpins. These observations are consistent with the auto-generation mechanism (Zhou *et al.* 1999; Adrian 2007; Kim *et al.* 2008).

Note that the route of late transition induced by the vortex ring with large vorticity flux and zero-twist in Case 4 is distinguished from the others induced by the twisted vortex ring. The initial vortex ring gradually dissipates and disappears in Case 4, without forming any other vortical structures at $t = 10$ in figure 9(*a*). It evolves into streamwise vortices near the outer layer at very late times in figure 9(*b*,*c*) and finally breaks down into turbulence in figure 9(*d*).

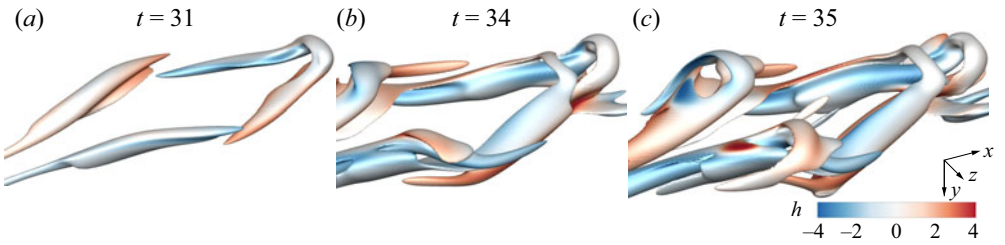

Figure 8. Evolution of the isosurface of $\lambda_{ci} = 1$ during the generation and evolution of hairpin vortices in Case 1. The isosurface is colour-coded by the helicity density. Note that the channel is flipped in the y-direction for clearly showing the vortical structure.

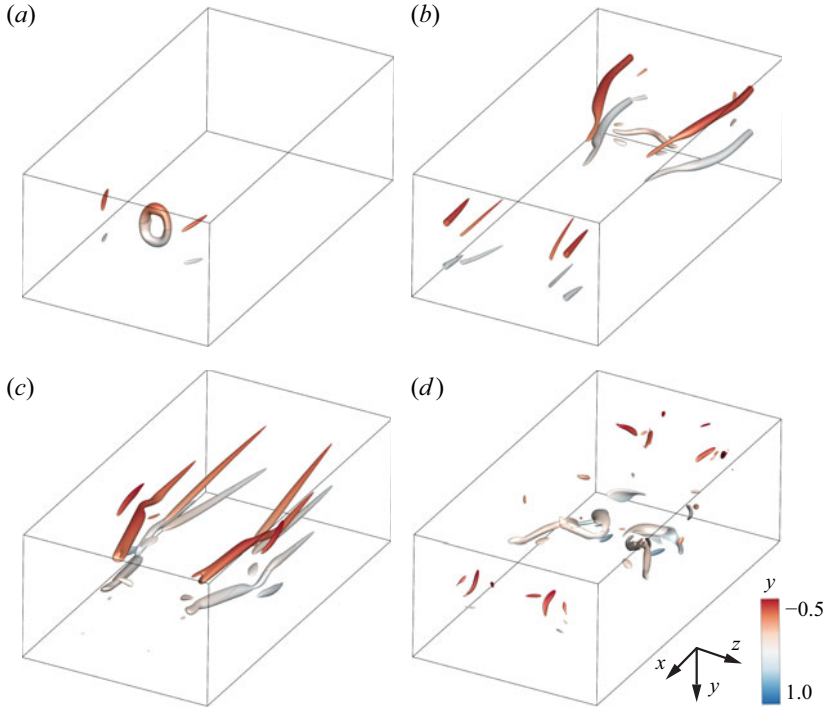

Figure 9. Evolution of the isosurface of λ_{ci} in Case 4: (*a*) $t = 10$ and $\lambda_{ci} = 1$; (*b*) $t = 20$ and $\lambda_{ci} = 0.7$; (*c*) $t = 30$ and $\lambda_{ci} = 0.5$; (*d*) $t = 50$ and $\lambda_{ci} = 2$. The surface is colour-coded by the wall distance.

3.2. *Transition induced by vortex bursting*

The internal dynamics of the vortex ring around $t_1 = 1$ is much faster than the disturbance growth in the boundary layer around $t_3 = 40$, so these two processes can be decoupled. The initial amplitude of the disturbance is determined by the dynamics of the vortex ring before t_1, whereas the subsequent linear amplification mechanism is mainly influenced by the background shear.

According to the rapid distortion theory (Sreenivasan & Narasimha 1978; Savill 1987; Nazarenko, Kevlahan & Dubrulle 1999; Deissler 2004), the amplitude of the disturbance is low in the early stage of transition, so the disturbance growth can be treated as inviscid. Moffatt (1967) applied the rapid distortion theory to the viscous sublayer (Saric *et al.*

2002) at $y^+ < 5$, where

$$y^+ = (1 - y)Re_\tau \tag{3.5}$$

is the normalised distance from the upper wall at $y = 1$, and the wall-normal length scale is much smaller than the streamwise one.

We consider the near-wall velocity $\boldsymbol{u}_B = (u_B, v_B, w_B)$ with

$$u_B = u(x, y^+, z), \quad v_B = v(x, y^+, z), \quad w_B = w(x, y^+, z), \quad y^+ < 5. \tag{3.6a–c}$$

Moffatt (1967) showed that when the disturbance amplitude is small, the streamwise disturbance mode $\hat{u}_B$ grows linearly with the wall-normal disturbance mode $\hat{v}_B$ as

$$\hat{u}_B(k_x, k_z) = \hat{u}_{B0}(k_x, k_z) - \mathcal{S}\hat{v}_B(k_x, k_z)t, \tag{3.7}$$

where $\hat{\cdot}$ denotes the Fourier transform of a quantity in the x–z plane with wavenumbers k_x and k_z, subscript 0 denotes the initial value and $\mathcal{S} = -2U_0 y$ is the shear rate of the Poiseuille flow. From (3.7), $\hat{v}_B$ is determined by the state around $t = t_1$, $\mathcal{S}$ is constant for a given y and $\hat{u}_B$ depends on $\hat{v}_B$, e.g. $\hat{u}_B$ increases with t for positive $-\mathcal{S}\hat{v}_B$.

We examine the evolution of $\hat{v}_B(k_{xz}, y^+)$ during the period of vortex bursting from t_{bs} to t_{be}, with $k_{xz} = \sqrt{k_x^2 + k_z^2}$. Based on the Parseval identity, we use

$$\overline{v_B^2}(y^+) = \frac{1}{A_{xz}} \iint v_B^2(x, y^+, z)\,\mathrm{d}x\,\mathrm{d}z = \sum_{k_{xz}} \hat{v}_B^2(k_{xz}, y^+) \tag{3.8}$$

to quantify the averaged amplitude of $\hat{v}_B$, where A_{xz} denotes the area of the x–z plane. Figure 10 plots the evolution of $\overline{v_B^2}(y^+ = 1)$ in Cases 1–3 in the very early stage when (3.7) is valid. Note that the evolution of $\overline{v_B^2}(y^+ = 5)$ is qualitatively the same (not shown). Case 2 has the lowest amplitude, and it has no transition. Cases 1 and 3 have larger amplitudes, suggesting the higher disturbance growth rate from (3.7), and both cases have transition. At early times, $\overline{v_B^2}(y^+ = 1)$ decays in Cases 2 and 3 due to the viscous effect, and its decay rate depends on the initial Γ. By contrast, $\overline{v_B^2}(y^+ = 1)$ grows by 15 % from t_{bs} to t_{be} in Case 1. The growth of v_B during the vortex bursting will be further discussed in § 4.

The transition is induced by the growth of v_B. According to (3.7), the streamwise disturbance of u_B grows with the vortex-ring induced v_B (Landahl 1975, 1980). The streaks are lifted by v_B in figure 7(*a*) and then elongated by the mean shear in figure 7(*b*), resulting in streamwise streaks downstream (Brandt & Henningson 2002). A hairpin vortex (Zhou *et al.* 1999) emerges from the streaks in figure 7(*c*), and then it evolves into a hairpin packet by the auto-generation mechanism (Adrian *et al.* 2000; Adrian 2007; Kim *et al.* 2008). The vortices break down and form a turbulent spot in figure 7(*d*), which eventually leads to a fully developed turbulent state (Wu 2023).

In summary, the threshold vorticity flux Γ^* is reduced from 0.231 in Case 4 to 0.0394 in Case 1 (see table 1) due to the induction of v_B in the vortex-ring evolution. In particular, the vortex bursting in Case 1 produces strong v_B near the boundary, enhancing the growth of u_B and then triggering a transition.

4. Induction of the wall-normal velocity in vortex bursting

4.1. *Introduction of the di-vorticity*

Next we elucidate the induction mechanism of v_B in the near-wall region by the large di-vorticity generated in the outer layer during the vortex bursting. The di-vorticity $\boldsymbol{\varrho} =$

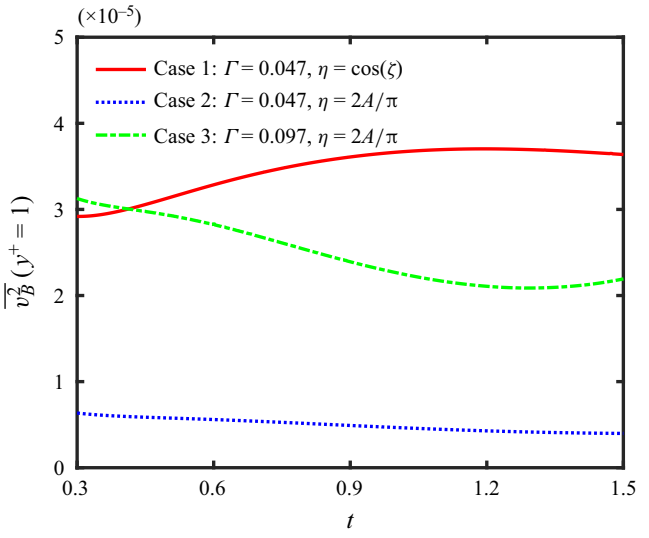

Figure 10. Evolution of $\overline{v_B^2}(y^+ = 1)$, as metric for the averaged amplitude of $\hat{v}_B(k_{xz}, y^+ = 1)$, from t_{bs} to t_{be} during the vortex bursting in Cases 1–3.

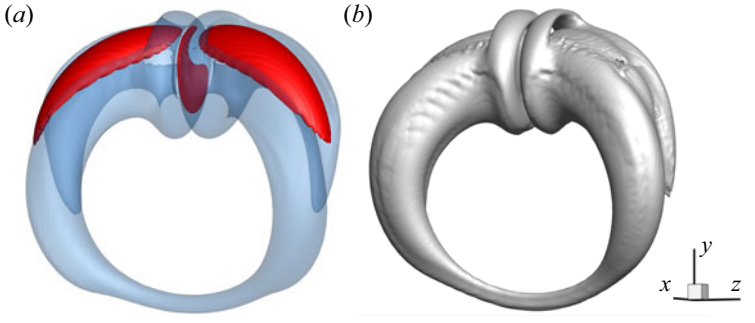

Figure 11. Reconstruction of the flow field using a small potion of the di-vorticity in Case 1 at $t = 0.9$. (*a*) Isosurface of $\lambda_{ci} = 2$ (blue) in the DNS, and isosurface of $|\boldsymbol{\varrho}| = 1000$ (red). (*b*) Isosurface of $\lambda_{ci} = 2$ in the flow field reconstructed from the di-vorticity in the region enclosed by the isosurface of $|\boldsymbol{\varrho}| = 1000$ (red surface in (*a*)). Note that this subdomain occupies only 0.2 % of V.

$\boldsymbol{\nabla} \times \boldsymbol{\omega}$ measures the local rotational intensity of the vorticity, and large $\boldsymbol{\varrho}$ may correspond to the local helical geometry of vortex lines. The identity $\nabla^2\boldsymbol{u} = \boldsymbol{\nabla}(\boldsymbol{\nabla} \cdot \boldsymbol{u}) - \boldsymbol{\varrho}$ suggests the Poisson equation

$$\nabla^2\boldsymbol{u} = -\boldsymbol{\varrho} \tag{4.1}$$

for the incompressible flow.

The di-vorticity has a very intermittent distribution in the transition. In Case 1, the maximum $|\boldsymbol{\varrho}|$ can be hundreds of times the volume-averaged $|\boldsymbol{\varrho}|$ during the vortex bursting. For example, at $t = 0.9$ in Case 1, the region with $|\boldsymbol{\varrho}| \geqslant 1000$ enclosed by the isosurface of $|\boldsymbol{\varrho}| = 1000$ occupies only 0.2 % of the volume of the entire channel in figure 11(*a*), but $\boldsymbol{\varrho}$ in this negligibly small region can reconstruct the vortical structure very close to the original in figure 11(*b*). Therefore, the highly concentrated $\boldsymbol{\varrho}$ near the site of vortex bursting can drive the near-wall flow dynamics in a finite time period after vortex bursting.

With higher-order velocity derivatives, $\boldsymbol{\varrho}$ has conservation constraints under given boundary conditions. The solid-wall boundary conditions are

$$\left.\begin{aligned} \boldsymbol{u} &= 0, \quad \boldsymbol{u} \in \partial\mathcal{V}, \\ \frac{\partial v}{\partial y} &= 0, \quad v \in \partial\mathcal{V}, \end{aligned}\right\} \tag{4.2}$$

which imposes the constraint

$$\int_{\mathcal{V}} y^n \varrho_y \mathrm{d}\mathcal{V} = 0, \quad n \in \mathbb{N} \tag{4.3}$$

on the di-vorticity. This constraint implies that the wall can have a response near the boundary to counter $\boldsymbol{\varrho}$ generated in a vortex-dynamics event remote from the wall. For $n = 0$, (4.3) suggests that the flow evolution only redistributes ϱ_y rather than changing the volume integration of ϱ_y. The implication of (4.3) will be further discussed in § 4.3.

4.2. *Generation of the di-vorticity during vortex bursting*

We demonstrate that large $\boldsymbol{\varrho}$ can be generated during the bursting of a vortex ring. The governing equation of $\boldsymbol{\varrho}$ is

$$\frac{\mathrm{D}\boldsymbol{\varrho}}{\mathrm{D}t} = \boldsymbol{\nabla} \times \boldsymbol{\nabla} \times \boldsymbol{a} + \boldsymbol{\omega} \cdot \boldsymbol{\nabla}\boldsymbol{\omega} + \boldsymbol{L}, \tag{4.4}$$

where $\boldsymbol{a} = -\boldsymbol{\nabla} p + \nabla^2 \boldsymbol{u}/Re$ denotes the acceleration of a fluid particle, and

$$\boldsymbol{L} \equiv (\boldsymbol{\nabla}\boldsymbol{\omega} \cdot \boldsymbol{\nabla}\boldsymbol{u} - \boldsymbol{\nabla}\boldsymbol{u} \cdot \boldsymbol{\nabla}\boldsymbol{\omega}) : \boldsymbol{\varepsilon} \tag{4.5}$$

has a form similar to the Lamb vector $\boldsymbol{\omega} \times \boldsymbol{u}$, with the Levi–Civita symbol $\boldsymbol{\varepsilon}$. On the right-hand side, the term $\boldsymbol{\nabla} \times \boldsymbol{\nabla} \times \boldsymbol{a}$ for the viscous effect can be neglected for very large Re, and then $\boldsymbol{\omega} \cdot \boldsymbol{\nabla}\boldsymbol{\omega}$ and $\boldsymbol{L}$ dominate the evolution of $\boldsymbol{\varrho}$.

Given the initial vortex ring in (2.5), the evolution of $\boldsymbol{\varrho}$ is estimated in curved cylindrical coordinates (s, ρ, θ). The vorticity-stretching and Lamb-like terms become (see Appendix B for a detailed derivation)

$$\boldsymbol{\omega} \cdot \boldsymbol{\nabla}\boldsymbol{\omega} = \left(0, 0, \omega_s \frac{1}{h_s}\frac{\partial \omega_\theta}{\partial s} + \omega_\theta \frac{1}{\rho}\frac{\partial \omega_\theta}{\partial \theta}\right) \tag{4.6}$$

and

$$\left.\begin{aligned} \boldsymbol{L} = \Bigg(& \frac{1}{\rho}\frac{\partial \omega_\theta}{\partial \rho}\frac{\partial u_\theta}{\partial \theta} - \frac{1}{h_s}\frac{\partial u_s}{\partial \rho}\frac{\partial \omega_\theta}{\partial s} - \frac{1}{\rho}\frac{\partial u_\theta}{\partial \rho}\frac{\partial \omega_\theta}{\partial \theta}, \\ & \frac{1}{\rho^2}\frac{\partial \omega_\theta}{\partial \theta}\frac{\partial u_s}{\partial \theta} - \frac{1}{h_s \rho}\frac{\partial \omega_\theta}{\partial s}\frac{\partial u_\theta}{\partial \theta} + \frac{1}{h_s^2}\frac{\partial u_s}{\partial s}\frac{\partial \omega_\theta}{\partial s}, \\ & -\frac{1}{h_s}\frac{\partial \omega_s}{\partial \rho}\frac{\partial u_s}{\partial s} - \frac{1}{\rho}\frac{\partial \omega_\theta}{\partial \rho}\frac{\partial u_s}{\partial \theta}\Bigg), \end{aligned}\right\} \tag{4.7}$$

respectively, where $h_s = 1 - \kappa\rho\cos\theta$ is the Lamé coefficient in the s-direction.

We analyse the variation of $\boldsymbol{\varrho}$ using (4.4) before t_1 when the vortex bursting occurs (see figure 4). In the model of η for a bursting vortex ring (Shen *et al.* 2023), the initial twist

distribution $\eta(s, t = 0) = A\cos(s/R)$ evolves into

$$\eta(s, \rho, t) = A\cos\left(\frac{s - B(\rho)\eta(s, \rho, t)t}{R}\right) \tag{4.8}$$

with $A = 120$ and $B = \Gamma\exp(-\rho^2/2\sigma^2)/(2\pi h_s)$, and (4.8) can be solved numerically using the explicit Newton method. Substituting (2.5) and (B2) into (4.8), we find that

$$\frac{\partial\omega_\theta}{\partial s} \sim \frac{\partial\eta}{\partial s} \quad \text{and} \quad \frac{\partial u_s}{\partial s} \sim \frac{\partial\eta}{\partial s} \tag{4.9a,b}$$

are dominant terms, where $\sim$ denotes an estimate of the order of magnitude. Other derivatives of $\boldsymbol{u}$ and $\boldsymbol{\omega}$ only depend on the initial configuration and remain constant during vortex bursting. With $\partial\eta/\partial s \gg \partial\eta/\partial\theta$ and $\partial\eta/\partial s \gg \partial\eta/\partial\rho$, we rank the magnitude of terms in (4.6) and (4.7) by $\partial\eta/\partial s$. By only keeping the dominant terms, (4.4) is approximated by

$$\frac{\mathrm{D}\boldsymbol{\varrho}}{\mathrm{D}t} \approx \frac{1}{h_s}\left(-\frac{\partial u_s}{\partial\rho}\frac{\partial\omega_\theta}{\partial s}, -\frac{1}{\rho}\frac{\partial\omega_\theta}{\partial s}\frac{\partial u_\theta}{\partial\theta} + \frac{1}{h_s}\frac{\partial u_s}{\partial s}\frac{\partial\omega_\theta}{\partial s}, \omega_s\frac{\partial\omega_\theta}{\partial s} - \frac{\partial\omega_s}{\partial\rho}\frac{\partial u_s}{\partial s}\right). \tag{4.10}$$

Here, the most influential term

$$I = \frac{1}{h_s^2}\frac{\partial u_s}{\partial s}\frac{\partial\omega_\theta}{\partial s} \sim \left(\frac{\partial\eta}{\partial s}\right)^2 \tag{4.11}$$

contains the product of two dominant terms. Finally, substituting (4.8) into (4.11), we estimate the order of (4.4) in terms of η as

$$\frac{\mathrm{D}\boldsymbol{\varrho}}{\mathrm{D}t} \approx I\boldsymbol{e}_\rho \sim \left(\frac{\partial\eta}{\partial s}\right)^2\boldsymbol{e}_\rho. \tag{4.12}$$

In figure 12, the distribution of $(\partial\eta/\partial s)^2$ along the s-direction shows that large $|\boldsymbol{\varrho}|$ is generated during vortex bursting and the di-vorticity is concentrated near the vortex bursting site at $s = \pi R/2$. The extremely twisted vortex lines, with the surge of $\partial\eta/\partial s$ in (4.12), manifest as the disc structure with large $|\boldsymbol{\varrho}|$ at $s = \pi R/2$ in figure 11(a).

4.3. *Induction of v_B*

From (3.7), we investigate the effect of ϱ_y, the most important component in $\boldsymbol{\varrho}$, on inducing v_B in the early transition. The Poisson equation (4.1) implies that although the large $\boldsymbol{\varrho}$ generated from vortex bursting is remote from the wall, it can have a strong induction effect in the entire domain, especially in the near-wall region.

To analyse v_B, we focus on (4.1) in the wall-normal direction

$$\left.\begin{aligned} \nabla^2 v &= -\varrho_y, \quad v \in \mathcal{V}, \\ v = 0 \quad \text{and} \quad \frac{\partial v}{\partial y} &= 0, \quad v \in \partial\mathcal{V}. \end{aligned}\right\} \tag{4.13}$$

This Poisson equation has a redundant boundary condition. We first consider only the Dirichlet boundary condition as

$$\left.\begin{aligned} \nabla^2 v &= -\varrho_y, \quad v \in \mathcal{V}, \\ v &= 0, \quad v \in \partial\mathcal{V}, \end{aligned}\right\} \tag{4.14}$$

and then treat the Neumann boundary condition as a boundary response to the vortices remote from the wall.

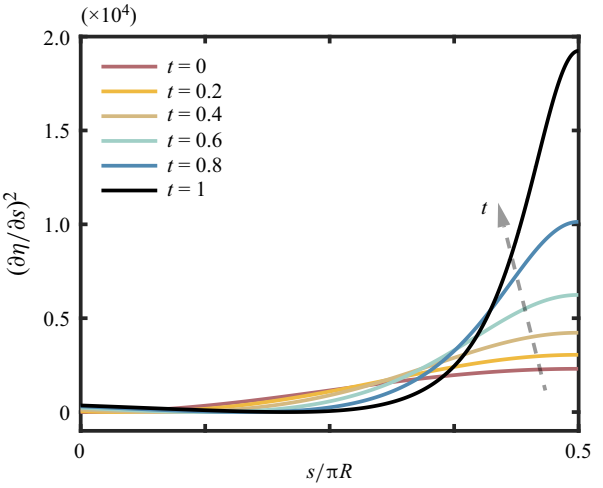

Figure 12. Evolution of $(\partial\eta/\partial s)^2$ in terms of the axial coordinate s along the centreline of the vortex ring during vortex bursting in Case 1.

We express the solution (see details in Appendix C)

$$v(\boldsymbol{x}) = \int_{\mathbb{R}^3} \varrho_y(\tilde{\boldsymbol{x}})\Phi(\boldsymbol{x}-\tilde{\boldsymbol{x}})\,\mathrm{d}\tilde{\boldsymbol{x}} \tag{4.15}$$

to (4.14) in terms of the fundamental solution

$$\Phi(\boldsymbol{x}) = \frac{1}{4\pi|\boldsymbol{x}|}, \tag{4.16}$$

where $\tilde{\boldsymbol{x}}$ and $\varrho_y(\tilde{\boldsymbol{x}})$ are extended quantities in $\mathbb{R}^3$ (see their definitions in Appendix C). As sketched in figure 13, (4.15) extends the integration region from the channel domain $\mathcal{V}$ to the entire 3-D space $\mathbb{R}^3$. As discussed in § 3, the vortex bursting triggers transition near the upper wall by inducing finite v_B. Without loss of generality, we consider the induction effect of ϱ_y near the upper wall at $\boldsymbol{x}_B = (x, y \to 1, z)$ based on (4.15).

The solution (4.15) to the Poisson equation can be simplified. The fundamental solution (4.16) decays at the rate of $|\boldsymbol{x}_B - \tilde{\boldsymbol{x}}|^{-1}$, so the induction effect can be neglected remote from the upper boundary except for the vortex-bursting disc $\mathcal{V}_{br}$ (marked in figure 13) where ϱ_y is concentrated. We approximate that only domains $\mathcal{V}$ and $\mathcal{V}_1$ in figure 13 contribute to the induction near $\boldsymbol{x}_B$ as

$$v_B(\boldsymbol{x}) \approx \int_{\mathcal{V}\cup\mathcal{V}_1} \varrho_y(\tilde{\boldsymbol{x}})\Phi(\boldsymbol{x}-\tilde{\boldsymbol{x}})\,\mathrm{d}\tilde{\boldsymbol{x}}, \quad \boldsymbol{x}\to\boldsymbol{x}_B \ \text{ and } \ \tilde{\boldsymbol{x}}\in\mathcal{V}\cup\mathcal{V}_1, \tag{4.17}$$

where $\mathcal{V}_1$ is the image domain adjacent to the upper boundary of $\mathcal{V}$.

Thus, the induction (4.15) from ϱ_y can be divided into two parts as

$$v_B \approx v_B^B + v_B^{br} \tag{4.18}$$

with

$$v_B^{br} = \int_{\mathcal{V}_{br}\cup\mathcal{V}_{1,br}} \varrho_y(\tilde{\boldsymbol{x}})\Phi(\boldsymbol{x}-\tilde{\boldsymbol{x}})\,\mathrm{d}\tilde{\boldsymbol{x}} = 2\int_{\mathcal{V}_{br}} \varrho_y(\tilde{\boldsymbol{x}})\Phi(\boldsymbol{x}-\tilde{\boldsymbol{x}})\,\mathrm{d}\tilde{\boldsymbol{x}} \tag{4.19}$$

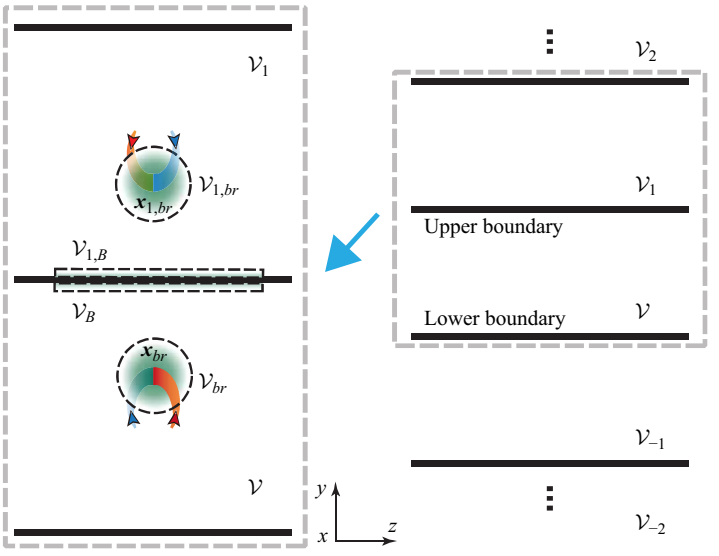

Figure 13. Schematic for extending the integration region of the Green function from the channel domain to the entire 3-D space. The extended domain consists of the original channel domain $\mathcal{V}$ and its mirror domains $\mathcal{V}_i$. The induction effect of ϱ_y in $\mathcal{V} \cup \mathcal{V}_1$ is shown on the left. The region with concentrated ϱ_y is coloured in green, including $\mathcal{V}_{br}$ near the site of vortex bursting and $\mathcal{V}_B$ near the upper boundary. The red and blue arrows denote twist vortex waves with opposite chiralities within the vortex ring in Case 1. The vortex bursts around $\boldsymbol{x}_{br} \in \mathcal{V}_{br}$ and generates large $\boldsymbol{\varrho}$ in the direction $\boldsymbol{e}_\rho$.

contributed from the bursting site and

$$v_B^B = \int_{\mathcal{V}_B \cup \mathcal{V}_{1,B}} \varrho_y(\tilde{\boldsymbol{x}}) \boldsymbol{\Phi}(\boldsymbol{x} - \tilde{\boldsymbol{x}}) \, \mathrm{d}\tilde{\boldsymbol{x}} = 2 \int_{\mathcal{V}_B} \varrho_y(\tilde{\boldsymbol{x}}) \boldsymbol{\Phi}(\boldsymbol{x} - \tilde{\boldsymbol{x}}) \, \mathrm{d}\tilde{\boldsymbol{x}}, \tag{4.20}$$

from the near-wall region $\mathcal{V}_B$. The two regions are coloured in green in figure 13.

First, we consider the induction effect in region $\mathcal{V}_{br}$ with the centre of vortex bursting at $\boldsymbol{x}_{br} = (x_{br}, y_{br}, z_{br})$. The multipole expansion (John 1998) is applied to (4.17), which is detailed in Appendix D. The approximation $(\tilde{\boldsymbol{x}} - \boldsymbol{x}_{br})/(\boldsymbol{x}_B - \boldsymbol{x}_{br}) \to \boldsymbol{0}$ holds in $\mathcal{V}_{br}$, satisfying the multipole assumption.

With the multipole expansion, the induction of

$$v_B^{br} = 2 \int_{\mathcal{V}_{br}} \varrho_y(\tilde{\boldsymbol{x}}) \boldsymbol{\Phi}(\boldsymbol{x}, \tilde{\boldsymbol{x}}) \, \mathrm{d}\tilde{\boldsymbol{x}} = \frac{1}{2\pi} \left(\frac{q_y}{|\boldsymbol{x} - \boldsymbol{x}_{br}|} + \frac{(\boldsymbol{x} - \boldsymbol{x}_{br}) \cdot \boldsymbol{p}_y}{|\boldsymbol{x} - \boldsymbol{x}_{br}|^3} + \cdots \right) \tag{4.21}$$

from ϱ_y in (4.19) is decomposed into the monopole

$$q_y = \int_{\mathcal{V}_{br}} \varrho_y(\tilde{\boldsymbol{x}}) \, \mathrm{d}\tilde{\boldsymbol{x}}, \tag{4.22}$$

the dipole

$$\boldsymbol{p}_y = \int_{\mathcal{V}_{br}} (\tilde{\boldsymbol{x}} - \boldsymbol{x}_{br}) \varrho_y(\tilde{\boldsymbol{x}}) \, \mathrm{d}\tilde{\boldsymbol{x}} \tag{4.23}$$

and high-order terms. Since q_y is concentrated in $\mathcal{V}_{br}$ and conserved in (4.3),

$$q_y \approx \int_{\mathcal{V}} \varrho_y(\tilde{\boldsymbol{x}}) \, \mathrm{d}\tilde{\boldsymbol{x}} = 0 \tag{4.24}$$

vanishes in (4.21). Then, (4.21) is simplified into

$$v_B^{br}(y,d) = \frac{1}{2\pi}\frac{(\boldsymbol{x}-\boldsymbol{x}_{br})\cdot\boldsymbol{p}_y}{|\boldsymbol{x}-\boldsymbol{x}_{br}|^3} = \frac{1}{2\pi}\frac{(y-y_{br})p_{y,y}}{(d^2+(y-y_{br})^2)^{3/2}} \tag{4.25}$$

with the only non-vanishing component $\boldsymbol{p}_y = (0, p_{y,y}, 0)$ and the distance $d = ((x - x_{br})^2 + (z - z_{br})^2)^{1/2}$ from the vortex-bursting site.

In the near-wall region $\mathcal{V}_B$, we re-express (4.25) in terms of y^+ as

$$v_B^{br}(y^+,d) = \frac{1}{2\pi}\frac{(1-y^+/Re_\tau - y_{br})p_{y,y}}{(d^2+(1-y^+/Re_\tau - y_{br})^2)^{3/2}}. \tag{4.26}$$

In the inner layer with $y^+ \ll Re_\tau$, (4.26) can be expanded around $y^+ = 0$ and linearised into

$$v_B^{br}(y^+,d) = \frac{1}{2\pi Re_\tau}\frac{y_{br}p_{y,y}}{(y_{br}^2+d^2)^{3/2}}\left(\frac{3y_{br}}{d^2+y_{br}^2} - \frac{1}{y_{br}}\right)y^+. \tag{4.27}$$

Thus, the value of v_B^{br} in (4.27) grows when the vortex bursts more closely to the upper wall, and it grows with y^+ linearly in the inner layer. The location (x_{br}, y_{br}, z_{br}) in (4.27) is determined by the initial vortex-ring disturbance, and the dipole strength $p_{y,y}$ is determined by the vortex evolution, which is discussed in § 4.2. Our DNS results show that larger Re_τ leads to smaller v_B (not shown), consistent with (4.27), and larger $p_{y,y}$, as implied by the larger disc in figure 4(*c*).

In addition to v_B^{br}, the wall-induced velocity v_B^B in (4.18) also contributes to v_B. In the evaluation of v_B^B in (4.20), the DNS result exhibits a very thin layer of ϱ_y in $\mathcal{V}_B$ as a response to the Neumann boundary condition (4.2). The averaged v_B^B is around a quarter of the averaged v_B^{br}.

The contours of v_B from the DNS and v_B^{br} from the model (4.27) are compared in figure 14. The approximation of v_B^{br} using (4.27) agrees with the DNS result of v_B, except that the averaged amplitude of v_B^{br} is 30 % smaller than v_B in the DNS. This discrepancy is primarily attributed to neglecting v_B^B in the model, with a minor contribution from neglecting the high-order terms in the multipole decomposition in (4.21). Therefore, (4.27) captures the dominant induction effect near the wall from the vortex evolution remote from the wall.

5. Conclusions

To study the influence of vortices remote from the boundary on the near-wall flow dynamics in wall-bounded flows, we have added a vortex ring with or without twist into the outer layer in a channel flow at $Re = 3333$. By elucidating the near-wall response to the vortex evolution, the vortex dynamics can shed light on the transition process of wall flows.

We have found that the initial twist of the vortex ring has an effect on the transition. By varying the vorticity flux and the local twist rate of the closed vortex tube, the minimum vorticity flux Γ^* for triggering transition is reduced by over 80 % from the initial disturbance of a vortex ring without twist ($\eta = 0$) to that with the differential twist ($\eta = A\cos(s/R)$). The flow evolution with the latter disturbance is featured by the vortex bursting in the early transitional stage.

The vortex-ring-induced transition in the channel flow is divided into three stages. Before $t_1 = 1$, the dynamics inside the vortex ring dominates. The vortex ring with

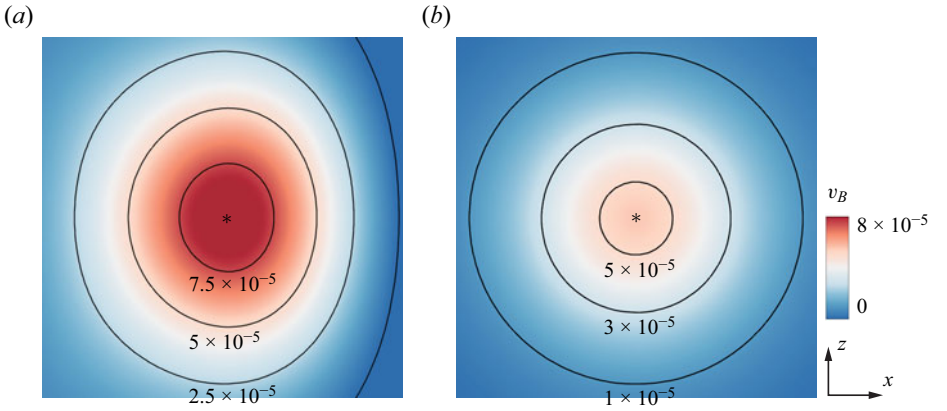

Figure 14. Contour of (*a*) v_B in the DNS and (*b*) v_B^{br} from the model in (4.27) in Case 1 in the x–z plane at $y^+ = 1$ and at $t = 1$ in Case 1. The asterisk marks the position of vortex bursting projected on the x–z plane.

differential twist in Case 1 undergoes the vortex bursting, whereas the vortex ring without twist in Case 4 only slightly deforms due to elliptic and curvature instabilities. From t_1 to $t_2 = 10$, the twisted vortex ring breaks up rapidly and evolves into the reversed hairpin vortex towards the inner layer; the untwisted vortex ring stays in the outer layer, preserves its shape and gradually dissipates. From t_2 to $t_3 = 40$, streamwise vortices form, and then break down into turbulence as in the classical route of transition.

We have characterised the influence of vortex evolution on transition using the near-wall, wall-normal velocity v_B with the rapid distortion theory. In the first stage around $t = t_1$, v_B grows by 15 % during the vortex-ring bursting in Case 1, whereas it remains constant or slightly decays in the absence of the vortex bursting. The enhanced v_B induces the higher growth rate of streamwise disturbances, leading to the streak formation followed by the transition.

We have introduced the di-vorticity $\boldsymbol{\varrho}$ to elucidate the interaction between inner and outer layers, and estimated the effect of large $\boldsymbol{\varrho}$ generated in vortex bursting on inducing v_B. During the vortex bursting, $\boldsymbol{\varrho}$ is concentrated within a compact, disc-like region near the vortex bursting site, and the large $\boldsymbol{\varrho}$ occupying a negligibility small volume can reconstruct the entire vortex structure with a satisfactory accuracy.

From the evolution equation of $\boldsymbol{\varrho}$ in the curved cylindrical coordinates, we have modelled the growing radial component of $\boldsymbol{\varrho}$ in terms of the local twist in (4.12), and demonstrate that the significant growth of $\boldsymbol{\varrho}$ is due to the generation of highly twisted vortex lines during vortex bursting. Then, we have derived that the generation of $\boldsymbol{\varrho}$ in the outer layer enhances v_B in the inner layer via the Poisson equation (4.13) with the image method and the multipole expansion. The estimation of v_B from our model in (4.27) qualitatively agrees with the DNS result.

In the future work, various vortex models which are more complex than the vortex ring can be applied to wall flows, and their induction effects on the near-wall dynamics can be studied via the di-vorticity. These studies can extend the vortex dynamics to the boundary-layer transition and flow control.

Acknowledgements. The authors thank W. Shen for helpful comments. Numerical simulations were carried out on the TH-2A supercomputer in Guangzhou, China.

Funding. This work has been supported by the National Natural Science Foundation of China (grant nos 11925201 and 11988102), the National Key R&D Program of China (grant no. 2020YFE0204200) and the Xplore Prize.

Declaration of interests. The authors report no conflict of interest.

Author ORCIDs.
Boyuan Wang https://orcid.org/0009-0004-7091-0576;
Yue Yang https://orcid.org/0000-0001-9969-7431.

Author contributions. Y.Y. and B.W. designed research. B.W. preformed research. B.W. and Y.Y. discussed the results and wrote the manuscript. All the authors have given approval for the manuscript.

Appendix A. Boundary correction on the initial vorticity

We impose the given $\boldsymbol{\omega}$ in (2.5) for a vortex ring into the background wall flow to generate the initial DNS field. However, the given vorticity can be incompatible with the boundary condition (4.2), so a boundary correction is applied.

The incompatibility is shown by the Biot–Savart law. The generalised Biot–Savart equation (Serrin 1959; Wu *et al.* 2007)

$$\boldsymbol{u}(\boldsymbol{x}) = \frac{1}{4\pi}\left(\int_{\mathcal{V}} \frac{\boldsymbol{\omega}\times(\boldsymbol{x}-\boldsymbol{x}')}{|\boldsymbol{x}-\boldsymbol{x}'|^3}\mathrm{d}\boldsymbol{x}' + \boldsymbol{P}\right), \quad \boldsymbol{x}'\in\mathcal{V} \tag{A1}$$

has rotational and irrotational parts, where the irrotational part $\boldsymbol{P}(\boldsymbol{x})$ depends on the boundary velocity. Applying the solid-wall boundary condition (4.2) to (A1), only the rotational part

$$\int_{\mathcal{V}} \frac{\boldsymbol{\omega}\times(\boldsymbol{x}-\boldsymbol{x}')}{|\boldsymbol{x}-\boldsymbol{x}'|^3}\mathrm{d}\boldsymbol{x}' = 0, \quad \boldsymbol{x}'\in\mathcal{V} \tag{A2}$$

remains at the boundary. Since the vorticity in (2.5) does not satisfy (A2), so a correction on (2.5) is necessary before the DNS.

In this appendix, we denote the vorticities before and after the boundary correction as $\boldsymbol{\omega}$ and $\boldsymbol{\omega}'$, respectively. To meet the Dirichlet boundary condition in (4.2), we consider the di-vorticity $\boldsymbol{\varrho} = (\varrho_x, \varrho_y, \varrho_z)$ instead of $\boldsymbol{\omega}$. Note that $\boldsymbol{\varrho}$ can uniquely determine $\boldsymbol{\omega}$ with (4.2) via the Poisson equation (4.1). According to the well-posedness of the Poisson equation, the boundary condition of $\boldsymbol{u}=0$ is sufficient to solve (4.1), and an extra Neumann boundary condition introduces the correction on $\boldsymbol{\varrho}$.

The boundary correction is based on the numerical method of Kim *et al.* (1987). It begins from the Poisson equation

$$\left.\begin{aligned} \nabla^2\varrho_y' &= \varrho_y, \quad \boldsymbol{x}\in\mathcal{V}, \\ \varrho_y' &= g, \quad \boldsymbol{x}\in\partial\mathcal{V} \end{aligned}\right\} \tag{A3}$$

for the y-component of $\boldsymbol{\varrho}$, where g denotes the boundary correction function to be determined, and $\boldsymbol{\varrho}' = \nabla\times\boldsymbol{\omega}' = (\varrho_x', \varrho_y', \varrho_z')$ the corrected di-vorticity. The correction in

(A3) is equivalent to the bi-harmonic equation

$$\left.\begin{aligned} \nabla^4 v &= 0, \quad \boldsymbol{x} \in \mathcal{V}, \\ \nabla^2 v &= -\varrho_y', \quad \boldsymbol{x} \in \mathcal{V}, \\ v &= 0, \quad \boldsymbol{x} \in \partial\mathcal{V}, \\ \frac{\partial v}{\partial y} &= 0, \quad \boldsymbol{x} \in \partial\mathcal{V}, \\ \nabla^2 v &= -g, \quad \boldsymbol{x} \in \partial\mathcal{V}. \end{aligned}\right\} \tag{A4}$$

Subsequently, other two velocity components are solved from the incompressible condition

$$\frac{\partial u}{\partial x} + \frac{\partial w}{\partial z} = -\frac{\partial v}{\partial y}, \tag{A5}$$

and then $\boldsymbol{\omega}'$ is calculated from $\boldsymbol{u}$.

To determine g, we first decompose

$$\left.\begin{aligned} v &= \sum_{m=1-(1/2)N_x}^{(1/2)N_x} \sum_{n=1-(1/2)N_z}^{(1/2)N_z} \hat{v}(m,n,y)\exp(\mathrm{i}\alpha_m x + \mathrm{i}\beta_n z), \\ \varrho_y &= \sum_{m=1-(1/2)N_x}^{(1/2)N_x} \sum_{n=1-(1/2)N_z}^{(1/2)N_z} \hat{\varrho}_y(m,n,y)\exp(\mathrm{i}\alpha_m x + \mathrm{i}\beta_n z), \\ \varrho_y' &= \sum_{m=1-(1/2)N_x}^{(1/2)N_x} \sum_{n=1-(1/2)N_z}^{(1/2)N_z} \hat{\varrho}_y'(m,n,y)\exp(\mathrm{i}\alpha_m x + \mathrm{i}\beta_n z), \\ g &= \sum_{m=1-(1/2)N_x}^{(1/2)N_x} \sum_{n=1-(1/2)N_z}^{(1/2)N_z} \hat{g}(m,n,\pm 1)\exp(\mathrm{i}\alpha_m x + \mathrm{i}\beta_n z) \end{aligned}\right\} \tag{A6}$$

into Fourier modes in x- and z-directions with $(m,n) \in \mathbb{Z}^2$ and $N_x = N_z = 256$. Then, (A3) is presented in the spectral form as the one-dimensional Helmholtz equations

$$\left.\begin{aligned} \left[-(\alpha_m^2 + \beta_n^2) + \frac{\mathrm{d}^2}{\mathrm{d}y^2}\right]\hat{\varrho}_y'(m,n,y) &= \hat{\varrho}_y(m,n,y), \\ \hat{\varrho}_y'(m,n,\pm 1) &= g(m,n,\pm 1), \\ \left[-(\alpha_m^2 + \beta_n^2) + \frac{\mathrm{d}^2}{\mathrm{d}y^2}\right]\hat{v}(m,n,y) &= \hat{\varrho}_y'(m,n,y), \\ \hat{v}(m,n,\pm 1) &= 0 \end{aligned}\right\} \tag{A7}$$

with the Dirichlet boundary conditions.

According to Kim *et al.* (1987), solutions to (A7) can be decomposed into the particular solution (with the subscript 'p') and the Neumann correction term (with the

subscript 'N') as

$$\left.\begin{aligned}\hat{\varrho}_y &= \varrho_p + \varrho_N,\\ \hat{v} &= v_p + v_N,\end{aligned}\right\} \tag{A8}$$

where ϱ_p denotes the solution to the inhomogeneous equation with the homogeneous boundary condition as

$$\left.\begin{aligned}\left[-(\alpha_m^2+\beta_n^2)+\frac{\mathrm{d}^2}{\mathrm{d}y^2}\right]\varrho_p(m,n,y) &= \hat{\varrho}_y(m,n,y),\\ \varrho_p(m,n,\pm1) &= 0,\\ \left[-(\alpha_m^2+\beta_n^2)+\frac{\mathrm{d}^2}{\mathrm{d}y^2}\right]v_p(m,n,y) &= \varrho_p(m,n,y),\\ v_p(m,n,\pm1) &= 0,\end{aligned}\right\} \tag{A9}$$

and ϱ_N denotes solution to the homogeneous equation with the inhomogeneous boundary condition as

$$\left.\begin{aligned}\left[-(\alpha_m^2+\beta_n^2)+\frac{\mathrm{d}^2}{\mathrm{d}y^2}\right]\varrho_N(m,n,y) &= 0,\\ \varrho_N(m,n,\pm1) &= \hat{g}(m,n,\pm1),\\ \left[-(\alpha_m^2+\beta_n^2)+\frac{\mathrm{d}^2}{\mathrm{d}y^2}\right]v_N(m,n,y) &= \varrho_N(m,n,y),\\ v_N(m,n,\pm1) &= 0.\end{aligned}\right\} \tag{A10}$$

For the bi-harmonic equations with the Dirichlet boundary conditions, (A9) can be solved numerically (Omrane, Ghedamsi & Khenissy 2016), and (A10) has the analytic solution

$$\left.\begin{aligned}\varrho_N &= \operatorname{csch}(2\lambda)(g(1)\sinh(\lambda(y+1))+g(-1)\sinh(\lambda(1-y))),\\ v_N &= \frac{\operatorname{csch}^2(2\lambda)}{4\lambda}(g(1)(y-1)\sinh(\lambda(y+3))+g(1)(y+3)\sinh(\lambda-\lambda y)\\ &\quad +g(-1)(y+1)\sinh(\lambda(y-3))-g(-1)(y-3)\sinh(\lambda(y+1)),\end{aligned}\right\} \tag{A11}$$

with shorthands $\lambda^2=\alpha_m^2+\beta_n^2$ and $g(\pm1)=\hat{g}(m,n,\pm1)$. Given v, the Neumann boundary condition of (A10)

$$\left.\begin{aligned}\frac{\mathrm{d}v_N(y=1)}{\mathrm{d}y} &= \frac{\operatorname{csch}^2(2\lambda)}{4\lambda}(g(1)(\sinh(4\lambda)-4\lambda)-2g(-1)\sinh(2\lambda)\\ &\quad +\ 4g(-1)\lambda\cosh(2\lambda)),\\ \frac{\mathrm{d}v_N(y=-1)}{\mathrm{d}y} &= -\frac{\operatorname{csch}^2(2\lambda)}{4\lambda}(-2g(1)\sinh(2\lambda)+4g(1)\lambda\cosh(2\lambda)\\ &\quad +\ g(-1)(\sinh(4\lambda)-4\lambda))\end{aligned}\right\} \tag{A12}$$

is expressed in terms of $g(\pm1)$, so $\hat{g}(m,n,\pm1)$ can be solved from $\mathrm{d}v_N/\mathrm{d}y(\pm1)$ analytically.

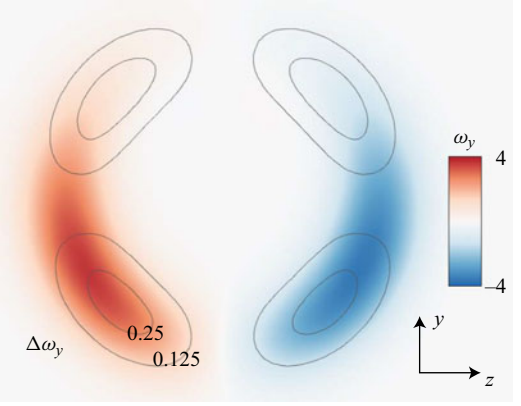

Figure 15. Contour of ω_y and contour lines of $\Delta\omega_y$ in the y–z plane at $x = L_x/2$ in Case 1 at $t = 0$.

From the Neumann boundary condition in (A4) and decomposition in (A8), the relation between $\mathrm{d}v_p/\mathrm{d}y(\pm 1)$ and $g(\pm 1)$ at the boundary is

$$\frac{\mathrm{d}v(\pm 1)}{\mathrm{d}y} = \frac{\mathrm{d}v_N(\pm 1)}{\mathrm{d}y} + \frac{\mathrm{d}v_p(\pm 1)}{\mathrm{d}y} = 0. \tag{A13}$$

With v_p solved in (A9), we obtain the boundary condition of v_N from (A13), and further g from (A12). With g, (A7) is then solved to obtain v_N. Finally, $\hat{v}$ is obtained from (A8), and then the corrected velocity for the DNS initial condition is obtained from (A6) and (A5).

We remark that the boundary correction has a negligible modification on the initial vorticity $\boldsymbol{\omega}$ in (2.5). For the most important vorticity component ω_y, we plot the distribution of the deviation $\Delta\omega_y = \omega_y' - \omega_y$ and ω_y' in the y–z plane at $x = L_x/2$ in figure 15. The largest deviation 0.329 is 4.75 % of the largest ω_y. The volume average of deviation $|\boldsymbol{\omega}' - \boldsymbol{\omega}|/|\boldsymbol{\omega}|$ is less than 0.1 %.

Appendix B. Di-vorticity generation inside the vortex ring

We analyse the axial velocity u_s and generation of the di-vorticity inside the vortex ring in the early stage. As sketched in figure 1, Xiong & Yang (2019) established a curved cylindrical frame $(\boldsymbol{e}_s, \boldsymbol{e}_\rho, \boldsymbol{e}_\theta)$ along a given curve $\mathcal{C}$ for the vortex centreline, with well-defined derivatives under the Frenet frame.

We focus on u_s inside the vortex ring. Under the axisymmetry of $\boldsymbol{\omega}$, only the azimuthal component ω_θ induces u_s. In (s, ρ, θ), the matrix form of $\boldsymbol{\omega}$ is

$$\omega_\theta = \frac{1}{\rho(1-\kappa\rho\cos\theta)} \begin{bmatrix} (1-\kappa\rho\cos\theta)\boldsymbol{e}_s & \boldsymbol{e}_\rho & \rho\boldsymbol{e}_\theta \\ \dfrac{\partial}{\partial s} & \dfrac{\partial}{\partial \rho} & \dfrac{\partial}{\partial \theta} \\ (1-\kappa\rho\cos\theta)u_s & 0 & 0 \end{bmatrix} \cdot \boldsymbol{e}_\theta. \tag{B1}$$

Solving (B1) yields

$$u_s = \frac{\Gamma\eta}{2\pi} \frac{1}{1-\kappa\rho\cos\theta} \exp\left(-\frac{\rho^2}{2\sigma^2}\right). \tag{B2}$$

The evolution equation (4.4) of $\boldsymbol{\varrho}$ is derived by taking curl of the vorticity equation

$$\frac{\mathrm{D}\boldsymbol{\omega}}{\mathrm{D}t} = \nabla \times \boldsymbol{a} + \boldsymbol{\omega} \cdot \nabla \boldsymbol{u} \tag{B3}$$

and using vector identities. Then, the generation of $\boldsymbol{\varrho}$ during vortex bursting is analysed. We rewrite velocity and vorticity gradient tensors in (4.5) in $(\boldsymbol{e}_s, \boldsymbol{e}_\rho, \boldsymbol{e}_\theta)$ as

$$\nabla \boldsymbol{u} = \begin{bmatrix} \dfrac{1}{1-\kappa\rho\cos\theta}\dfrac{\partial u_s}{\partial s} & 0 & 0 \\ \dfrac{\partial u_s}{\partial \rho} & 0 & \dfrac{\partial u_\theta}{\partial \rho} \\ \dfrac{1}{\rho}\dfrac{\partial u_s}{\partial \theta} & 0 & \dfrac{1}{\rho}\dfrac{\partial u_\theta}{\partial \theta} \end{bmatrix} \tag{B4}$$

and

$$\nabla \boldsymbol{\omega} = \begin{bmatrix} 0 & 0 & \dfrac{1}{1-\kappa\rho\cos\theta}\dfrac{\partial \omega_\theta}{\partial s} \\ \dfrac{\partial \omega_s}{\partial \rho} & 0 & \dfrac{\partial \omega_\theta}{\partial \rho} \\ 0 & 0 & \dfrac{1}{\rho}\dfrac{\partial \omega_\theta}{\partial \theta} \end{bmatrix}, \tag{B5}$$

respectively, where $\partial u_\theta/\partial s = 0$, $\partial \omega_s/\partial s = 0$ and $\partial \omega_s/\partial \theta = 0$ are applied under symmetries. Substituting (B4) and (B5) into (4.5), we have (4.6) and (4.7).

Appendix C. Green function for channel flow

We derive (4.15) from the Poisson equation with the Dirichlet boundary condition (4.14) by extending the channel domain $\mathcal{V}$ to the entire 3-D space $\mathbb{R}^3$. This extension removes the boundary effect and simplifies the mathematical representation.

First, we establish the Green function for a channel domain. Start from the general Green function in $\mathcal{V}$

$$G(\boldsymbol{x}, \boldsymbol{x}') \equiv \Phi(\boldsymbol{x} - \boldsymbol{x}') - \phi(\boldsymbol{x}, \boldsymbol{x}'), \quad \boldsymbol{x}, \boldsymbol{x}' \in \mathcal{V}, \boldsymbol{x} \neq \boldsymbol{x}', \tag{C1}$$

where Φ is the fundamental solution of the Poisson equation (4.16), and $\phi(\boldsymbol{x}, \boldsymbol{x}')$ is a corrector for the boundary condition as

$$\left.\begin{aligned} \nabla'^2 \phi(\boldsymbol{x}, \boldsymbol{x}') = 0, \quad \boldsymbol{x} \in \mathcal{V}, \quad \forall \boldsymbol{x} \in \mathcal{V}, \\ \phi(\boldsymbol{x}, \boldsymbol{x}') = \Phi(\boldsymbol{x}' - \boldsymbol{x}), \quad \boldsymbol{x} \in \partial\mathcal{V}, \quad \forall \boldsymbol{x} \in \mathcal{V}, \end{aligned}\right\} \tag{C2}$$

where ∇ and ∇' are the derivatives with respect to $\boldsymbol{x}$ and $\boldsymbol{x}'$, respectively. The Green function (C2) can be rewritten in the equivalent differential form

$$\left.\begin{aligned} \nabla^2 G(\boldsymbol{x}, \boldsymbol{x}') = -\delta(\boldsymbol{x} - \boldsymbol{x}'), \quad \boldsymbol{x} \in \mathcal{V}, \\ G(\boldsymbol{x}, \boldsymbol{x}') = 0, \quad \boldsymbol{x} \in \partial\mathcal{V}. \end{aligned}\right\} \tag{C3}$$

For a channel bounded by planes $y = 1$ and $y = -1$, we define the reflection point

$$\tilde{\boldsymbol{x}}_1 = (x, 2 - y, z) \in \mathcal{V}_1 \tag{C4}$$

of $\boldsymbol{x} \in \mathcal{V}$ with respect to $y = 1$, and the reflection point

$$\tilde{\boldsymbol{x}}_{-1} = (x, -2 - y, z) \in \mathcal{V}_{-1} \tag{C5}$$

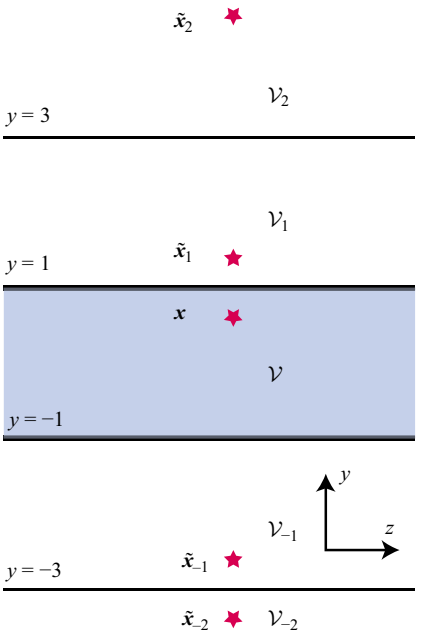

Figure 16. Schematic for reflection points in image domains with respect to $\boldsymbol{x}$ in the channel.

with respect to $y = -1$. Reflecting points $\tilde{\boldsymbol{x}}_1$ and $\tilde{\boldsymbol{x}}_{-1}$ again with respect to planes $y = \mp 1$ yields

$$\tilde{\boldsymbol{x}}_2 = (x, y + 4, z) \in \mathcal{V}_2 \quad \text{and} \quad \tilde{\boldsymbol{x}}_{-2} = (x, y - 4, z) \in \mathcal{V}_{-2}, \tag{C6a,b}$$

respectively. As sketched in figure 16, the subscript of $\tilde{\boldsymbol{x}}$ denotes the image domain where the refection point is located. In this way, we generate a set of reflection points

$$\left.\begin{aligned} \tilde{\boldsymbol{x}}_k &= (x, -y + 2k, z), \quad \text{for odd } k, \\ \tilde{\boldsymbol{x}}_k &= (x, y + 2k, z), \quad \text{for even } k. \end{aligned}\right\} \tag{C7}$$

Then, we define the Green function

$$G(\boldsymbol{x}, \boldsymbol{x}') = \frac{1}{4\pi} \sum_{k \in \mathbb{Z}} \frac{(-1)^k}{|\boldsymbol{x}' - \tilde{\boldsymbol{x}}_k|} \tag{C8}$$

for a channel from (C1) and (C7) with the image method (Roach 1982). It suggests that the effect of the wall is equal to a set of image points. The Green function (C8) is well-defined, because substituting (C7) into (C8) satisfies (C3).

The solution

$$v(\boldsymbol{x}) = -\int_{\partial \mathcal{V}} v \frac{\partial G}{\partial y} \mathrm{d}S + \int_{\mathcal{V}} \varrho_y(\boldsymbol{x}') G(\boldsymbol{x}, \boldsymbol{x}') \, \mathrm{d}\boldsymbol{x}', \quad \boldsymbol{x}, \boldsymbol{x}' \in \mathcal{V} \tag{C9}$$

to (4.14) can be written in terms of the Green function $G(\boldsymbol{x}, \boldsymbol{x}')$ of (4.14). Applying the solid-wall boundary condition to (C9) yields

$$v(\boldsymbol{x}) = \int_{\mathcal{V}} \varrho_y(\boldsymbol{x}') G(\boldsymbol{x}, \boldsymbol{x}') \, \mathrm{d}\boldsymbol{x}'. \tag{C10}$$

Next, we extend v in $\mathcal{V}$ to $\mathbb{R}^3$ by setting a map of $\boldsymbol{\varrho}$ from $\mathcal{V}$ to $\mathbb{R}^3$. Define the projection between $\mathcal{V}$ and $\mathcal{V}_k$

$$\forall k \in \mathbb{Z}, f_k : \mathcal{V} \to \mathcal{V}_k, \quad \boldsymbol{x} \mapsto \tilde{\boldsymbol{x}}_k. \tag{C11a,b}$$

Then, define each reflected $\boldsymbol{\varrho}(\tilde{\boldsymbol{x}})$ in $\mathcal{V}_k$,

$$\forall k \in \mathbb{Z}, \boldsymbol{\varrho}_k : V_k \to \mathbb{R}^3, \quad \tilde{\boldsymbol{x}}_k \mapsto (-1)^k \boldsymbol{\varrho}(f_k^{-1}(\tilde{\boldsymbol{x}}_k)). \tag{C12a,b}$$

Finally, unite all $\mathcal{V}_k$ into $\mathbb{R}^3$ as $\bigcup_{k\in\mathbb{Z}} \mathcal{V}_k = \mathbb{R}^3$, and define $\boldsymbol{\varrho}(\tilde{\boldsymbol{x}})$ in $\mathbb{R}^3$ by $\boldsymbol{\varrho}_k(\tilde{\boldsymbol{x}})$ in $\mathcal{V}_k$ as

$$\forall k \in \mathbb{Z}, \boldsymbol{\varrho}(\tilde{\boldsymbol{x}}) = \boldsymbol{\varrho}_k(\tilde{\boldsymbol{x}}), \quad \tilde{\boldsymbol{x}} \in \mathcal{V}_k. \tag{C13}$$

With the extended field $\boldsymbol{\varrho}(\tilde{\boldsymbol{x}})$ in (C13), the solution (4.15) to the Poisson equation (4.13) can be written in the integral form in $\mathbb{R}^3$.

Appendix D. Multipole expansion

We provide the detailed derivation of (4.21). Consider a compact field $\boldsymbol{\varrho}(\boldsymbol{x})$ in $\mathcal{V} \subseteq \mathbb{R}^3$ with $\boldsymbol{\varrho}(\boldsymbol{x}) \to 0$ and $|\boldsymbol{x}| > d_c$, where d_c is a constant. The induced field

$$\boldsymbol{u}(\boldsymbol{x}) = \frac{1}{4\pi} \int_{\mathcal{V}} \boldsymbol{\varrho}(\tilde{\boldsymbol{x}}) \frac{1}{|\boldsymbol{x} - \tilde{\boldsymbol{x}}|} \mathrm{d}\tilde{\boldsymbol{x}} \tag{D1}$$

via the Poisson equation $\nabla^2 \boldsymbol{u} = -\boldsymbol{\varrho}(\boldsymbol{x})$ is the superposition of the fundamental solution (4.16). For $|\tilde{\boldsymbol{x}} - \boldsymbol{x}| \gg d_c$, $\boldsymbol{u}$ can be expanded into a Taylor series.

The canonical Taylor expansion for a vector function $\boldsymbol{f}(\tilde{\boldsymbol{x}})$ around $\tilde{\boldsymbol{x}} = \boldsymbol{x}_0$ is

$$\boldsymbol{f}(\tilde{\boldsymbol{x}}) = \boldsymbol{f}(\boldsymbol{x}_0) + (\tilde{\boldsymbol{x}} - \boldsymbol{x}_0) \cdot \nabla \boldsymbol{f}(\tilde{\boldsymbol{x}})|_{\boldsymbol{x}_0} + \tfrac{1}{2}((\tilde{\boldsymbol{x}} - \boldsymbol{x}_0) \cdot \nabla)^2 \boldsymbol{f}(\tilde{\boldsymbol{x}})|_{\boldsymbol{x}_0} + \cdots. \tag{D2}$$

Setting $f(\tilde{\boldsymbol{x}}) = 1/|\tilde{\boldsymbol{x}} - \boldsymbol{x}|$ and $\boldsymbol{x}_0 = \boldsymbol{x}_{br}$ and ignoring the second- and higher-order terms, (D2) becomes

$$\frac{1}{|\tilde{\boldsymbol{x}} - \boldsymbol{x}|} = \frac{1}{|\boldsymbol{x}_{br} - \boldsymbol{x}|} + (\tilde{\boldsymbol{x}} - \boldsymbol{x}_{br}) \cdot \left(-\frac{\boldsymbol{x}_{br} - \boldsymbol{x}}{|\boldsymbol{x} - \boldsymbol{x}_{br}|^3} \right) + \cdots. \tag{D3}$$

Then, multiplying (D3) by $\boldsymbol{\varrho}(\tilde{\boldsymbol{x}})$ and then integrating by $\tilde{\boldsymbol{x}}$ in $\mathcal{V}$, we have

$$\int_{\mathcal{V}} \boldsymbol{\varrho}(\tilde{\boldsymbol{x}}) \frac{1}{|\boldsymbol{x} - \tilde{\boldsymbol{x}}|} \mathrm{d}\tilde{\boldsymbol{x}} = \int_{\mathcal{V}} \frac{\boldsymbol{\varrho}(\tilde{\boldsymbol{x}})}{|\boldsymbol{x} - \boldsymbol{x}_{br}|} \mathrm{d}\tilde{\boldsymbol{x}} + \int_{\mathcal{V}} \boldsymbol{\varrho}(\tilde{\boldsymbol{x}})(\tilde{\boldsymbol{x}} - \boldsymbol{x}_{br}) \cdot \left(\frac{\boldsymbol{x} - \boldsymbol{x}_{br}}{|\boldsymbol{x} - \boldsymbol{x}_{br}|^3} \right) \mathrm{d}\tilde{\boldsymbol{x}} + \cdots. \tag{D4}$$

Finally, taking the y-component of $\boldsymbol{\varrho}$, setting $\mathcal{V} = \mathcal{V}_{br}$ and multiplying (D4) by $1/4\pi$ yields (4.21).

References

Adrian, R.J. 2007 Hairpin vortex organization in wall turbulence. *Phys. Fluids* **19**, 041301.

Adrian, R.J., Meinhart, C.D. & Tomkins, C.D. 2000 Vortex organization in the outer region of the turbulent boundary layer. *J. Fluid Mech.* **422**, 1–54.

Archer, P.J., Thomas, T.G. & Coleman, G.N. 2008 Direct numerical simulation of vortex ring evolution from the laminar to the early turbulent regime. *J. Fluid Mech.* **598**, 201–226.

Arendt, S., Fritts, D.C. & Andreassen, Ø. 1997 The initial value problem for Kelvin vortex waves. *J. Fluid Mech.* **344**, 181–212.

Blanco-Rodríguez, F.J. & Dizès, S.L. 2017 Curvature instability of a curved Batchelor vortex. *J. Fluid Mech.* **814**, 397–415.

BOIKO, A.V., WESTIN, K.J.A., KLINGMANN, B.G.B., KOZLOV, V.V. & ALFREDSSON, P.H. 1994 Experiments in a boundary layer subjected to free stream turbulence. Part 2. The role of TS-waves in the transition process. *J. Fluid Mech.* **281**, 219–245.

BRANDT, L. & HENNINGSON, D.S. 2002 Transition of streamwise streaks in zero-pressure-gradient boundary layers. *J. Fluid Mech.* **472**, 229–261.

CANUTO, C., HUSSAINI, M.Y., QUARTERONI, A. & ZANG, T.A. 1988 *Spectral Methods in Fluid Dynamics*. Springer.

CHENG, M., LOU, J. & LIM, T.T. 2010 Vortex ring with swirl: a numerical study. *Phys. Fluids* **22**, 097101.

CUYPERS, Y., MAUREL, A. & PETITJEANS, P. 2003 Vortex burst as a source of turbulence. *Phys. Rev. Lett.* **91**, 194502.

DAZIN, A., DUPONT, P. & STANISLAS, M. 2006 Experimental characterization of the instability of the vortex rings. Part 2. Non-linear phase. *Exp. Fluids* **41**, 401–413.

DEISSLER, R.G. 2004 Effects of inhomogeneity and of shear flow in weak turbulent fields. *Phys. Fluids* **4**, 1187–1198.

FARRELL, B.F. & IOANNOU, P.J. 2012 Dynamics of streamwise rolls and streaks in turbulent wall-bounded shear flow. *J. Fluid Mech.* **708**, 149–196.

FRANSSON, J.H.M., MATSUBARA, M. & ALFREDSSON, P.H. 2005 Transition induced by free-stream turbulence. *J. Fluid Mech.* **527**, 1–25.

FUKUMOTO, Y. & HATTORI, Y. 2005 Curvature instability of a vortex ring. *J. Fluid Mech.* **526**, 77–115.

HAIDARI, A.H. & SMITH, C.R. 1994 The generation and regeneration of single hairpin vortices. *J. Fluid Mech.* **277**, 135–162.

HE, G.-S., WANG, J.-J., PAN, C., FENG, L.-H., GAO, Q. & RINOSHIKA, A. 2017 Vortex dynamics for flow over a circular cylinder in proximity to a wall. *J. Fluid Mech.* **812**, 698–720.

HOF, B., JUEL, A. & MULLIN, T. 2003 Scaling of the turbulence transition threshold in a pipe. *Phys. Rev. Lett.* **91**, 244502.

HUNT, J.C.R. & DURBIN, P.A. 1999 Perturbed vortical layers and shear sheltering. *Fluid Dyn. Res.* **24**, 375.

HUSSAIN, F. 1986 Coherent structures and turbulence. *J. Fluid Mech.* **173**, 303–356.

JACOBS, R.G. & DURBIN, P.A. 2001 Simulations of bypass transition. *J. Fluid Mech.* **428**, 185–212.

JI, L. & VAN REES, W.M. 2022 Bursting on a vortex tube with initial axial core-size perturbations. *Phys. Rev. Fluids* **7**, 044704.

JOHN, D.J. 1998 *Classical Electrodynamics*, 3rd edn. Wiley.

KERSWELL, R.R. 2002 Elliptical instability. *Annu. Rev. Fluid Mech.* **34**, 83–113.

KIM, J., MOIN, P. & MOSER, R. 1987 Turbulence statistics in fully developed channel flow at low Reynolds number. *J. Fluid Mech.* **177**, 133–166.

KIM, K., ADRIAN, R.J., BALACHANDAR, S. & SURESHKUMAR, R. 2008 Dynamics of hairpin vortices and polymer-induced turbulent drag reduction. *Phys. Rev. Lett.* **100**, 134504.

LANDAHL, M.T. 1975 Wave breakdown and turbulence. *SIAM J. Appl. Maths*. **28** (4), 735–756.

LANDAHL, M.T. 1980 A note on an algebraic instability of inviscid parallel shear flows. *J. Fluid Mech.* **98**, 243–251.

LUCKRING, J.M. 2019 The discovery and prediction of vortex flow aerodynamics. *Aeronaut. J.* **123**, 729–804.

MELANDER, M.V. & HUSSAIN, F. 1994 Core dynamics on a vortex column. *Fluid Dyn. Res.* **13**, 1–37.

MOFFATT, H.K. 1967 The interaction of turbulence with strong wind shear. In *Proc. URSI-IUGG Int. Colloq. Atmos. Turbul. Radio Wave Propag.*, pp. 139–154. Nauka.

MULLIN, T. 2011 Experimental studies of transition to turbulence in a pipe. *Annu. Rev. Fluid Mech.* **43**, 1–24.

NAZARENKO, S., KEVLAHAN, N.K.-R. & DUBRULLE, B. 1999 WKB theory for rapid distortion of inhomogeneous turbulence. *J. Fluid Mech.* **390**, 325–348.

OLSTHOORN, J. & DALZIEL, S.B. 2015 Vortex-ring-induced stratified mixing. *J. Fluid Mech.* **781**, 113–126.

OMRANE, H.B., GHEDAMSI, M. & KHENISSY, S. 2016 Biharmonic equations under Dirichlet boundary conditions with supercritical growth. *Adv. Nonlinear Stud.* **16**, 175–184.

PEIXINHO, J. & MULLIN, T. 2006 Decay of turbulence in pipe flow. *Phys. Rev. Lett.* **96**, 094501.

PHILIPPE, R.S., ROBERT, D.M. & MICHAEL, M.R. 1991 Spectral methods for the Navier–Stokes equations with one infinite and two periodic directions. *J. Comput. Phys.* **96**, 297–324.

RICCO, P., LUO, J. & WU, X. 2011 Evolution and instability of unsteady nonlinear streaks generated by free-stream vortical disturbances. *J. Fluid Mech.* **677**, 1–38.

ROACH, G.F. 1982 *Green's Functions*. Cambridge University Press.

RUBIN, Y., WYGNANSKI, I.J. & HARITONIDIS, J.H. 1980 Further observations on transition in a pipe. In *Laminar-Turbulent Transition; Proc. IUTAM Symp. Stuggart, FRG, 1979* (ed. R. Eppler & F. Hussein), pp. 19–26. Springer.

SAFFMAN, P.G. 1981 Dynamics of vorticity. *J. Fluid Mech.* **106**, 49–58.

SANDHAM, N.D. & KLEISER, L. 1992 The late stages of transition to turbulence in channel flow. *J. Fluid Mech.* **245**, 319–348.
SARIC, W.S., REED, H.L. & KERSCHEN, E.J. 2002 Boundary-layer receptivity to freestream disturbances. *Annu. Rev. Fluid Mech.* **34**, 291–319.
SAVILL, A.M. 1987 Recent developments in rapid-distortion theory. *Annu. Rev. Fluid Mech.* **19**, 531–573.
SCHLATTER, P., STOLZ, S. & KLEISER, L. 2004 LES of transitional flows using the approximate deconvolution model. *Intl J. Heat Fluid Flow* **25**, 549–558.
SCHOPPA, W. & HUSSAIN, F. 2002 Coherent structure generation in near-wall turbulence. *J. Fluid Mech.* **453**, 57–108.
SERRIN, J. 1959 *Mathematical Principles of Classical Fluid Mechanics*, pp. 125–263. Springer.
SHARIFF, K. & LEONARD, A. 1992 Vortex rings. *Annu. Rev. Fluid Mech.* **24**, 235–279.
SHEN, W., YAO, J., HUSSAIN, F. & YANG, Y. 2022 Topological transition and helicity conversion of vortex knots and links. *J. Fluid Mech.* **943**, A41.
SHEN, W., YAO, J., HUSSAIN, F. & YANG, Y. 2023 Role of internal structures within a vortex in helicity dynamics. *J. Fluid Mech.* **970**, A26.
SREENIVASAN, K.R. & NARASIMHA, R. 1978 Rapid distortion of axisymmetric turbulence. *J. Fluid Mech.* **84**, 497–516.
WU, J.Z., MA, H. & ZHOU, M.-D. 2007 *Vorticity and Vortex Dynamics*. Springer.
WU, X. 2019 Nonlinear theories for shear flow instabilities: physical insights and practical implications. *Annu. Rev. Fluid Mech.* **51**, 451–485.
WU, X. 2023 New insights into turbulent spots. *Annu. Rev. Fluid Mech.* **55**, 45–75.
WU, X., JACOBS, R.G., HUNT, J.C.R. & DURBIN, P.A. 1999 Simulation of boundary layer transition induced by periodically passing wakes. *J. Fluid Mech.* **398**, 109–153.
XIONG, S. & YANG, Y. 2019 Construction of knotted vortex tubes with the writhe-dependent helicity. *Phys. Fluids* **31**, 047101.
XU, J., LIU, J., ZHANG, Z. & WU, X. 2023 Spatial–temporal transformation for primary and secondary instabilities in weakly non-parallel shear flows. *J. Fluid Mech.* **959**, A21.
YANG, Y. & PULLIN, D.I. 2011 Geometric study of Lagrangian and Eulerian structures in turbulent channel flow. *J. Fluid Mech.* **674**, 67–92.
ZAKI, T.A. 2013 From streaks to spots and on to turbulence: exploring the dynamics of boundary layer transition. *Flow Turbul. Combust.* **91**, 451–473.
ZAKI, T.A. & DURBIN, P.A. 2005 Mode interaction and the bypass route to transition. *J. Fluid Mech.* **531**, 85–111.
ZHAO, Y., XIONG, S., YANG, Y. & CHEN, S. 2018 Sinuous distortion of vortex surfaces in the lateral growth of turbulent spots. *Phys. Rev. Fluids* **3**, 074701.
ZHAO, Y., YANG, Y. & CHEN, S. 2016 Evolution of material surfaces in the temporal transition in channel flow. *J. Fluid Mech.* **793**, 840–876.
ZHONG, X. & WANG, X. 2012 Direct numerical simulation on the receptivity, instability, and transition of hypersonic boundary layers. *Annu. Rev. Fluid Mech.* **44**, 527–561.
ZHOU, J., ADRIAN, R.J. & BALACHANDAR, S. 1996 Autogeneration of near-wall vortical structures in channel flow. *Phys. Fluids* **8**, 288–290.
ZHOU, J., ADRIAN, R.J., BALACHANDAR, S. & KENDALL, T.M. 1999 Mechanisms for generating coherent packets of hairpin vortices in channel flow. *J. Fluid Mech.* **387**, 353–396.